

Nd:Al₂O₃ as a Gain Material for Integrated Devices

M.Sc thesis

Koop van Dalzen
August 2009

Department of Applied Physics



University of Twente
The Netherlands

Nd:Al₂O₃ as a gain material for integrated devices

Master's thesis
Master of Science, Applied Physics
August 2009

Koop (Marko) van Dalfsen

Department of Applied Physics
University of Twente

Graduation committee:

Prof. dr. Markus Pollnau (IOMS)

Dr. Kerstin Wörhoff (IOMS)

Dr. Feridun Ay (IOMS)

Prof. dr. Klaus Boller (LF)

This work has been performed at IOMS:

Integrated Optics and MicroSystems

MESA+ Institute for Nanotechnology

Faculty of Electrical Engineering, Mathematics and Computer Science

University of Twente

P.O. Box 217

7500 AE Enschede

Acknowledgments

During the past nine months I've had the opportunity to conclude my study of Applied Physics in an optics research group: a research field I never thought I'd end up in, as the field of optics never had much appeal to me in my early studies. I was however wrong in thinking that the field of optics was boring, as many intriguing processes have been, and have yet to be discovered in optical physics. My interest in nano- and microfabrication in combination with the enthusiasm for optics exhibited by Markus Pollnau during many of his lectures have in the end pushed me into the direction of integrated optics: a field that will see extreme amounts of development in decades to come.

This thesis could not have been written without the support of many people. From the IOMS group I would first like to thank Markus Pollnau for having me in this group and for having faith in a successful ending of this M.Sc thesis. I also would like to thank you for your offer to continue my work as a Ph.D student in the IOMS group. I would like to thank Kerstin Wörhoff for her support especially during the last weeks of my thesis and making sure I didn't overwork myself. Feridun: I could not have done my work without the continuous feedback from you and you keeping up the good mood. *Bir elin nesi var iki elin sesi var!* You just make sure you don't *oversmoke* yourself! I sincerely would like to thank Jing Yang for her help with the gain measurements and correcting my early thesis chapters. Also I will never randomly place chips on a mask again, I promise!

I am also much indebted to Dimitri for much help with free-space optics and just for being relaxed. I thank you and Saara-Maarit for correcting part of the thesis. I would like to thank Laura for her help with life-time measurements and discussions about the integrated laser design. Here, I also have to thank Edward for help on this topic. I also would like to thank Jonathan for his *prima* lasers, discussions about the rings, scripts and making sure I didn't take up too much work. I have to thank Henk for his help with the high-resolution SEM images. I also have to thank the technicians Meindert for etching the Al_2O_3 waveguides and Gabriël for dicing. I also need to thank Anton for much help and support with setups. Rita, thanks for making sure everything with respect to arranging the graduation was properly taken care of.

Though not actively involved in my project, I would like to thank the other members of the IOMS group for their friendship and I hope I will get to know you better in the next years: Abu, Chaitanya, Lasse, Fehmi, Fei, René, Hugo, So, Nur and Imran. Also a good luck to Marcel writing your Ph.D thesis and Christos with your continuing work in Southampton!

I would like to thank Klaus Boller for taking part in the committee as the external committee member.

From my friends of the RSK I would like to thank Aleida, Jolanda, Ronald, Herbert, Ferdinand and Hans for their friendship and support during the last year. Also I would like to thank my roommate Albert for his friendship and support, as well as reading part of my

early thesis.

I am very grateful for my family and the support they have given me throughout my studies. I am especially grateful for their prayers. I also have to thank family Van den Berg for the exact same reason.

Finally I would like to thank Esther, who has been my biggest source of support and love during this graduation work. I could not have done it without you!

Marko van Dalzen
Enschede, August 2009

Contents

Acknowledgments	iii
1 Introduction	1
1.1 Integrated optics and its applications	1
1.2 Integrated optical circuits	1
1.3 Al ₂ O ₃ , a promising material for integrated optics	2
1.4 Overview of this thesis	2
2 Gain in Nd:Al₂O₃	3
2.1 Introduction	3
2.2 Theory	3
2.2.1 The Nd ion	3
2.2.2 Level populations in thermal equilibrium	4
2.2.3 Absorption and stimulated emission	5
2.2.4 Small signal gain	6
2.3 Experimental setup	8
2.4 Simulations	9
2.4.1 Free-space to channel-mode overlap	9
2.5 Experimental results	10
2.6 Conclusions	11
3 Nd as a laser ion	13
3.1 Introduction	13
3.2 Laser theory	13
3.2.1 Radiative and non-radiative emission	13
3.2.2 Secondary processes	14
3.2.3 Rate equations	14
3.2.4 The laser cavity	15
3.2.5 Laser threshold	15
3.3 Simulation of Nd-doped Al ₂ O ₃ lasers	16
3.4 Simulation results	16
3.5 Conclusions	18
4 Waveguides and couplers	21
4.1 Introduction	21
4.2 Theory	21
4.2.1 Waveguides	21

4.2.2	Directional coupler	23
4.2.3	Mach-Zehnder coupler (or balanced coupler)	24
4.3	Simulations	25
4.3.1	Simulation procedure and software	25
4.3.2	Waveguide mode analysis and calculations	26
4.3.3	Couplers	26
4.4	Experimental setup	28
4.4.1	Coupler measurements	28
4.4.2	SEM imaging	29
4.5	Results	30
4.5.1	Coupler measurements	30
4.5.2	Coupler SEM analysis	31
4.6	Conclusions	32
5	Integrated optical reflectors for waveguide lasers	33
5.1	Introduction	33
5.2	Theory	33
5.2.1	Bend losses	33
5.2.2	Passive mirrors	34
5.2.3	The Sagnac mirror	34
5.3	Simulations	35
5.3.1	Bend losses	35
5.3.2	Sagnac mirror	35
5.4	Conclusions	37
6	Design of on-chip laser devices	39
6.1	Introduction	39
6.2	Exploring different laser designs	39
6.2.1	Sagnac-pumped integrated waveguide laser	39
6.2.2	Cavity-pumped integrated waveguide laser	40
6.2.3	Ringlaser	41
6.3	Laser parametrization	41
6.3.1	Waveguide dimensions and cavity length	41
6.3.2	Mirror reflectivities	42
6.3.3	Signal-out couplers	43
6.4	Conclusions	44
	Conclusions	45
	Bibliography	47
	Appendices	51
A	Integrated laser designs	51
A.1	General information	52
A.2	Loop mirrors	53
A.3	Ringlaser	54
A.4	Long Sagnac laser I	55

A.5 Long Sagnac laser II	57
A.6 Short Sagnac laser I	58
A.7 Short Sagnac laser II	59
B Laser simulation parameters	61

Chapter 1

Introduction

1.1 Integrated optics and its applications

Integrated optics, in which optical devices are fabricated on a chip, is a rapidly expanding field. Integrated optics differs from free-space optics in the way that functions that would otherwise need bulky equipment in free-space optics, are combined on a single chip. Light is confined within on-chip lightguides, called 'channel waveguides'. The concept of guiding optical signals in lightguides is known since the early sixties. It was not until the late sixties and early seventies, however, that the importance of integrated optics was realized [1], leading to the first topical meeting on integrated optics in 1972 [2]. Low-cost optical fibers developed in the early 1980's have led to gradual replacement of metallic wires for telecommunication. Meanwhile, improvements in micro- and nanolithography technology led to the introduction of integrated on-chip optical circuits. Integrated optical circuits have many applications in communications and sensing. In particular, Neodymium-doped (Nd) materials have applications in communications because of its emission in the second telecommunication window. Various sensing applications and lab-on-a-chip systems not limited to this specific Nd-ion have been proposed and are being investigated [3–6], and will become common in years to come.

1.2 Integrated optical circuits

For integrated optics, a material is required that is transparent for the wavelength of light that we intend to guide and this light must not be allowed to escape this material or be absorbed in the material. This material is usually embedded within another material, or air, having lower *refractive indices*. Light can be confined in the high-refractive-index material by exploiting *total internal reflection*, in which light reflects internally at the interface between the high refractive index material and the low refractive index material. By confining light in a thin layer and cascading several structures to manipulate the flow of light, an integrated optical chip can be developed. Examples of structures to manipulate the flow of light are waveguide directional couplers [7], used to couple light from one waveguide to another and Bragg reflectors to reflect light in a waveguide [8, 9]. In this thesis, we will study and design directional couplers for use in integrated laser devices. Instead of Bragg reflectors, we will use Sagnac mirrors to reflect light in a waveguide [10].

1.3 Al₂O₃, a promising material for integrated optics

In 1986 a new material, Al₂O₃, for integrated optics was demonstrated, with a higher refractive index than competitive glass materials, low losses, and high transparency over a wide wavelength range [11]. Much research has been done on this material by IOMS and other research groups. At IOMS, this material has been optimized for use in integrated optics, by developing a way to etch this material and to obtain low-loss channel waveguides [12]. Various rare-earth ions such as Er³⁺ and Nd³⁺ can be implanted in this material to obtain optical gain at wavelengths native to these ions. Al₂O₃ is an amorphous material and is compatible with silicon-based technology. Due to the amorphous nature of the material, a broad emission spectrum is obtained. Its high refractive index allows for small integrated devices, as the bending radii of such devices can be reduced compared to devices produced in other lower-index materials. Furthermore, since the material can be deposited on SiO₂ layers, it can be fully integrated with other silicon-based devices and can easily be patterned using standard lithography and etching procedures. In this thesis, we will focus on Nd-doped Al₂O₃ to study the optical gain at a wavelength of 1064 nm that can be achieved in this material. In case sufficient gain can be obtained, the possibility to design integrated amplifiers and integrated lasers opens up.

1.4 Overview of this thesis

Chapter 2 will focus on the gain in Nd-doped Al₂O₃. The theory of gain will be explained and experimental gain results will be discussed and compared to gain obtained in other materials. In Chapter 3 we will study an integrated Nd-doped Al₂O₃ waveguide laser by simulations. In Chapter 4, waveguide channels and couplers will be investigated by simulations and compared to experimental results. In Chapter 5, the topic of integrated waveguide mirrors will be treated. Finally, Chapter 6 will discuss the design of integrated channel waveguide lasers.

Chapter 2

Gain in Nd:Al₂O₃

2.1 Introduction

Optical gain on the Nd³⁺ transition at 1064 nm in Nd-doped Al₂O₃ channel waveguides has been investigated and will be discussed in this chapter. If sufficient gain is obtained this is interesting for Nd³⁺ integrated amplifiers and integrated lasers in the Al₂O₃ host material. Optical gain in Nd-doped channel waveguides has previously been reported for various host materials and different waveguide fabrication methods: a LiNbO₃ host material with channels fabricated by proton-exchange, yielding 7.5 dB of gain in a 5.6 mm long channel [13], or 1.5 dB/cm in Nd:glass with laser-written channels [14]. More recently, gain has been demonstrated in Nd-doped sol-gel-based channel waveguides yielding 3.75 dB/cm of optical gain [15], and polymer-based channel waveguides yielding 1.4 dB/cm of optical gain [16]. In this chapter, the theory about the gain mechanisms in an active material, such as absorption of pump light and stimulated emission leading to signal amplification, will be discussed. The experiment for measuring the gain will be explained and the obtained results will be discussed and compared to gain results reported in the literature.

2.2 Theory

2.2.1 The Nd ion

Gain in a passive material is achieved by incorporating active material into the passive material. In this thesis, we will investigate optical gain in Nd-doped Al₂O₃. Neodymium (Nd) is a rare-earth ion, with an electronic structure (Xe)4f⁴5d⁰6s². Nd can be implanted in Al₂O₃, replacing an Al ion. When a Nd ion is inserted into a host material, the 6s electrons and one of the 4f electrons is used for binding, making the Nd-ion a triply ionized ion (Nd³⁺). The remaining 4f electrons cause a large number of energy levels. The Nd ions are implanted in the Al₂O₃ by co-sputtering, while growing the Al₂O₃ layer.[18] These rare-earth ions are pumped into a higher energy state, and subsequently release their energy upon being triggered by a signal photon. Figure 2.1 shows the energy diagram of the Nd ion and it behaves like a four-level system with the ⁴F_{3/2} level having a significantly longer lifetime than the ⁴F_{5/2} level or the levels below the ⁴F_{3/2} level in Figure 2.1. Radiative emission from this level terminates on the ⁴I_{11/2} level, one level above the ground level. The simplest lasing energy diagram includes pumping from the ⁴I_{9/2} ground level into the ⁴F_{5/2} level. The short lifetime

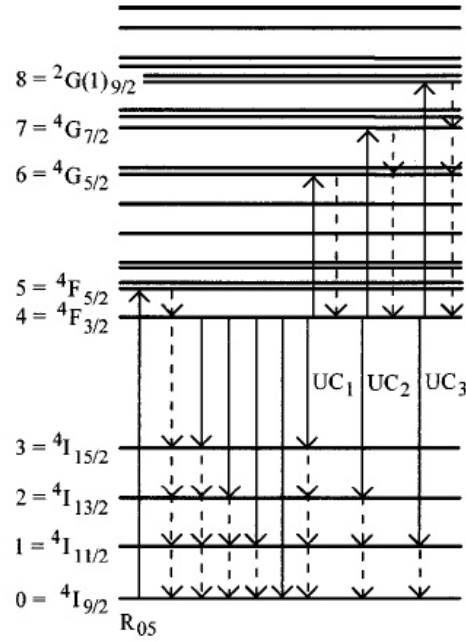


Figure 2.1: Energy levels of the Nd-ion. Arrows in the figure from left to right denote, respectively: pump transition at 800 nm, cascaded multiphonon relaxations, various fluorescent transitions from the ${}^4F_{3/2}$ upper laser level, and upconversion (UC) processes. [17]

of this level, due to phonon relaxation, causes near-immediate nonradiative decay into the long lifetime ${}^4F_{3/2}$ laser level. Radiative decay from the ${}^4F_{3/2}$ level into the ${}^4I_{11/2}$ level is rapidly followed by nonradiative decay to the ${}^4I_{9/2}$ ground level.

2.2.2 Level populations in thermal equilibrium

For atoms in thermal equilibrium, the population density ratio of two arbitrary levels with population densities N_1 and N_2 in [m^{-3}], and energy E_1 and E_2 is described by Boltzmann statistics:

$$\frac{N_2}{N_1} = \frac{g_2}{g_1} \exp\left[\frac{E_1 - E_2}{k_B T}\right], \text{ with } E_2 > E_1 \quad (2.1)$$

where g_1 and g_2 denote the degeneracies of the levels, k_B is the Boltzmann constant and T is the temperature. In case of a degenerate level, for example a level that has a degeneracy of $g = 2$, both degenerate levels are at the same energy level and have to share the total population. Note however that the total population has also increased because the probability for an ion to occupy the upper level has also doubled! The total population density N_i is the sum of the population densities N_{ij} of N_i , j being a sublevel of i :

$$N_i = \sum_{j=1}^{g_i} N_{ij} \quad (2.2)$$

Consider a material with an amount of N_T ions. In thermal equilibrium, level populations decrease with increasing level energy. The fraction of ions in an arbitrary level N_i can be

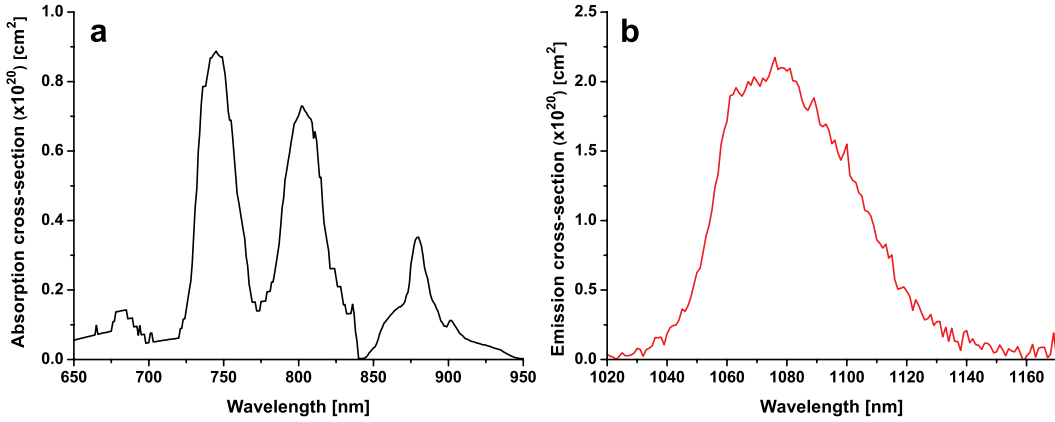


Figure 2.2: Absorption (σ_a) and emission (σ_e) cross-sections for the Nd ion, measured using spectroscopy. Nd in Al_2O_3 has a strong absorption peak around $\lambda = 800$ nm, and a strong emission peak around $\lambda = 1064$ nm. [19]

calculated by:

$$f_i = \frac{g_i \exp[-E_i/k_B T]}{\sum_{j=1}^n g_j \exp[-E_j/k_B T]} \quad (2.3)$$

so that the population N_i equals $N_i = f_i N_T$.

2.2.3 Absorption and stimulated emission

Consider an ensemble of ions, with population density N_T in thermal equilibrium, ie. no external effects are present. A simplified case is considered with only two energy levels so that $N_T = N_0 + N_1$, ie. an ion can either occupy level 0 or 1. In thermal equilibrium, most of the ions occupy the ground-state and a marginal fraction occupies the higher energy level according to Boltzmann theory described in the previous section. When electromagnetic radiation in the form of photons is introduced, additional ions make a transition from the ground-state to a higher energy state corresponding to the energy of the incident photons. This process, known as absorption, is for this 2-level system described by: [20]

$$\frac{dN_1}{dt} = W_{01}N_0 = -\frac{dN_0}{dt} \quad (2.4)$$

Here, the rate of change of ions leaving the ground level 0 equals the rate of change of ions excited into the higher energy level 1. From eqn. 2.4 it is clear that the rate of absorption increases with N_0 ie. the absorption is stronger when a higher fraction of ions occupy the ground-state. The absorption rate coefficient W_{01} depends on the incident field intensity and the probability that an ion absorbs a photon. The coefficient W_{01} has a dimension of $[s^{-1}]$ and can be written as:

$$W_{01} = \sigma_{01}F_{01} \quad (2.5)$$

where F_{01} is the photon flux in [$m^{-2}s^{-1}$] and σ_{01} is the absorption cross-section in [m^2]. For the Nd four-level system discussed below, the absorption coefficient is called σ_a rather than σ_{01} .

The reverse process, known as stimulated emission, can be described with similar equations for a transition from the upper energy state to the lower energy state. The rate of change of stimulated emission depends on the amount of ions in the upper energy state:

$$\frac{dN_0}{dt} = W_{10}N_1 = -\frac{dN_1}{dt} \quad (2.6)$$

The coefficient W_{10} represents the stimulated emission rate coefficient and has the same form as equation 2.5:

$$W_{10} = \sigma_{10}F_{10} \quad (2.7)$$

where σ_{10} is called the emission cross-section and F_{10} is once again the photon flux. For the Nd four-level system discussed below, the emission coefficient is called σ_e rather than σ_{10} . The photon flux has been purposely written with the indices because for a multilevel system, rather than the simplified 2-level system discussed here, the photon flux F_{01} represents the pump photons and F_{10} represents signal photons and these need not be equal. For a simple 2-level system, $F_{01} = F_{10} = F$

2.2.4 Small signal gain

Equations 2.4 and 2.6 describe absorption and emission. For every absorption and emission event, one photon is annihilated or created, respectively. The change in photon flux dF therefore equals the sum of the rates of change times the propagation length dz :

$$\begin{aligned} dF &= [W_{10}N_1 - W_{01}N_0] dz \\ dF &= \sigma F [N_1 - N_0] dz \end{aligned} \quad (2.8)$$

The second equation arises from the fact that for a 2-level system, $W_{01} = W_{10} = W$ and $\sigma_{01} = \sigma_{10} = \sigma$. Equation 2.8 reveals that for a positive flux change dF , $N_1 > N_0$. This condition is called 'inversion', when more ions occupy the upper level so that the stimulated emission rate exceeds the absorption rate. A photon flux F now increases to $F + dF$ over a distance dz and gain is achieved. The gain coefficient for this 2-level system is:

$$g = \sigma(N_1 - N_0) \quad (2.9)$$

For the described 2-level system gain can never be achieved, because for a system in thermal equilibrium the absorption and stimulated emission rates are equal. This means that the system is transparent as any photon that gets absorbed is re-emitted. The solution is using a 3-level or a 4-level system. Key to these systems is that the energy level at which the pump transition terminates, differs from the level from which the laser transition originates. The level from which the laser transition originates acts as an intermediate, buffer, level due to its long lifetime. The energy stored in this buffer level can be extracted by stimulated emission, leading to signal amplification. The first two arrows in the Nd 4-level system of Figure 2.1 represent the pump and signal transitions, respectively, the ${}^4F_{3/2}$ acting as the buffer level. Since the pump terminating level, ${}^4F_{5/2}$, makes a rapid transition to the buffer level it can be considered empty with the respect to the ${}^4I_{9/2}$ ground level. Pump photon

absorption is hence not limited by the population density of the pump terminating level as was the case for the 2-level system, but solely depends on the pump photon flux and ${}^4\text{I}_{9/2}$ ground level population.

For the 4-level system in Figure 2.1, the population density of level ${}^4\text{F}_{3/2}$, called N_2 , can be written as:

$$\frac{dN_2}{dt} = R_p - WN_2 - \frac{N_2}{\tau} \quad (2.10)$$

where R_p is the pump rate, which excites ions from the ground-state into level 3. A rapid transition from level 3 to level 2 then follows. W is the stimulated emission rate and $1/\tau$ represents the combined rates of radiative and non-radiative emission from the N_2 level to lower levels. The steady-state level population of level 2, putting $dN_2/dt = 0$, reads:

$$N_2 = \frac{R_p\tau}{1 + W\tau} = \frac{N_{20}}{1 + I/I_s} \quad (2.11)$$

where N_{20} is the population of level 2 when no signal photons are present, and hence no stimulated emission. $I = Wh\nu/\sigma_e$ is the signal photon intensity and $I_s = h\nu/\sigma\tau$. I_s represents the signal intensity for which the level population N_2 gets saturated. The signal intensity to achieve saturation is defined as the intensity that causes the population density N_2 to drop to $\frac{1}{2}N_{2I}$. Here, N_{2I} is the level population in level 2 at a certain pump rate, when no signal photons are present. Now that the level populations are known, equation 2.11 can be rewritten into an equation that gives the gain as function of the signal intensity, using equation:

$$g = \frac{g_0}{1 + I/I_s} \quad (2.12)$$

Here, $g_0 = \sigma_e N_{20} = \sigma_e R_p \tau$ is the 'small signal gain', also called 'unsaturated gain coefficient'. The small signal gain is the maximum possible gain in a material for a given pump power. As the signal intensity I increases, an increasing amount of ions in level 2 will fall back to the ground level, reducing the population in level 2 and hence reducing gain. The small signal gain can therefore be thought of as the gain experienced by a single signal photon passing through a pumped material, when no other signal photons are present.

As light travels through a channel it is subject to losses due to scattering and absorption. If the channel is doped with active material and if this material is pumped, light intensity will also be enhanced. The intensity I as a function of the total loss coefficient α and the gain coefficient g , at a propagation length L is given by:

$$I(L) = I_0 e^{(g-\alpha)L} \quad (2.13)$$

The gain in a channel can now be determined using:

$$g = \frac{10}{L} \log_{10} \left[\frac{I}{I_0} \right] + \alpha \quad (2.14)$$

where the gain coefficient g and the total loss coefficient α are given in [dB/cm] and L in [cm]. I_0 is the intensity in the channel at $L = 0$. This equation requires knowledge of the intensity in the channel at the start and at the end. The gain coefficient g is not to be confused with the net gain g_{net} , which is the the gain in a channel after subtraction of the loss value α . The net gain equals $g_{\text{net}} = g - \alpha$.

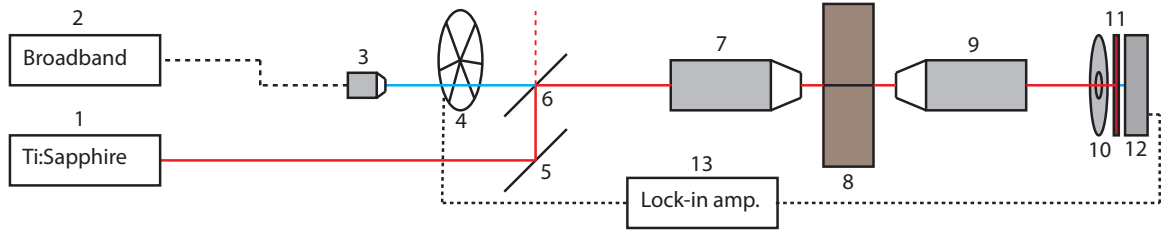


Figure 2.3: Diagram of the setup used to measure small signal gain on 1-cm-long Nd:Al₂O₃ channels. The numbered components are: 1) Ti:Sapphire pump source at $\lambda = 800$ nm 2) signal source at $\lambda = 1064$ nm 3) fiber lens 4) chopper at 133 Hz 5) 100% mirror at pump wavelength 6) piece of glass, to transmit signal light and partially reflect pump light 7) 60x, NA=0.85 objective lens 8) 1 cm long Nd:Al₂O₃ channels 9) 20x, NA=0.40 objective lens 10) pinhole 11) high-pass filter, cut-off at $\lambda = 850$ nm 12) Germanium detector 13) lock-in amplifier connecting chopper and detector

2.3 Experimental setup

Small signal gain in 1-cm-long Nd-doped channels was measured using a Ti:Sapphire laser (Spectra-Physics 3900S) as a pump source at 800 nm. The beam from the Ti:Sapphire pump source was expanded to twice its diameter to maximize filling of the used incoupling microscope lens. The beam expander used was a Galilean type beam expander using a 40 mm plano-concave lens in combination with an 80 mm acromatic lens. To probe the gain of the channels for signal wavelength at 1064 nm, a Nd:YAG broadband light source (Fianium) was used at its lowest power to minimize wavelength broadening around its peak at $\lambda = 1064$ nm. Light from this broadband light source was coupled into a standard 9/125 fiber (Thorlabs) and refocused to a beam using a fiber lens. Pump and signal beams were then combined by two mirrors. The combined signal and pump light was coupled into the $2.0 \times 0.6 \mu\text{m}$, NA = 0.81, uncladded channels using a NA = 0.85 objective lens of 60 \times magnification. Light exiting the channels was refocused onto a Germanium detector using a NA = 0.40 microscope lens of 20 \times magnification. To ensure collection of channel light alone, a pinhole was put in front of the detector. Residual pump light was filtered out using a high-pass wavelength filter with cut-off at $\lambda = 850$ nm. During the measurement, signal light was chopped at a frequency of 133 Hz. The pump light was unchopped, but blocked and unblocked during subsequent measurements. The signal intensity was read off the lock-in amplifier, both when the active medium was pumped and unpumped. Integration times of the lock-in amplifier used for the gain measurement was 300 ms at the minimum, up to 1 s. The gain coefficient g in equation 2.14 could be measured directly according to:

$$g = \frac{10}{L} \log_{10} \frac{I_p}{I_{u.p.}} - \alpha \quad (2.15)$$

where I_p is the measured signal intensity for the pumped case, and $I_{u.p.}$ for the unpumped case.

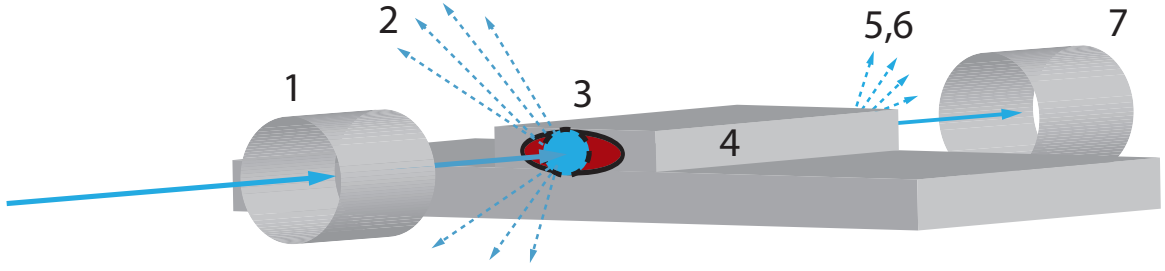


Figure 2.4: Diagram of a channel waveguide between two incoupling microscope lenses. In order to estimate the launched power inside the channel, one needs to know all loss values indicated by the numbers. The losses introduced when light is incoupled into a channel and outcoupled again are, respectively: 1) incoupling microscope lens efficiency 2) losses due to reflection at the material - air interface plus additional losses due to facet roughness 3) overlap mismatch between the Gaussian pump beam and channel mode profiles 4) channel loss due to absorption and scattering 5,6) overlap mismatch, reflection and facet roughness losses at outcoupling interface 7) outcoupling microscope lens efficiency.

2.4 Simulations

2.4.1 Free-space to channel-mode overlap

In order to know the amount of pump power within the channels, one needs to know the coupling efficiencies. Pump light coming from a laser source is often assumed to have a Gaussian shape. To approximate the pump power within the channel, also called 'launched power', we also assume a Gaussian beam shape. This light is focussed into the channel using an objective lens with a certain numerical aperture, Figure 2.4. The beam waist obtained after the lens can be approximated by:

$$W_0 = \frac{2\lambda_0}{n\pi\text{NA}} \quad (2.16)$$

where NA is the numerical aperture of the focussing (objective) lens, n is the refractive index which equals $n = 1$ in our case, and λ_0 is the free-space wavelength [21].

The objective lens focusses the beam to a much smaller beam waist W_0 in the focal point, at the cost of a large divergence angle. Coupling between a channel mode and a free-space Gaussian beam depends on their overlap. If, for example, the beam waist W_0 matches the mode field diameter (MFD) of the fundamental mode in the channel, we end up with a theoretical 100% coupling, excluding losses due to reflection.

The MFD's for the channel geometries used in our gain measurements have been calculated. These MFD's have been split into a horizontal and a vertical component because the shape of the fundamental mode in these channels is not circular but elliptical. The channels measured have no upper SiO₂ cladding. The channel dimensions are $2.0 \times 0.6 \mu\text{m}$ (width \times height) and are shallow etched by an amount of 100 nm. The overlap values between the channel fundamental modes and the beam waist W_0 , given by equation 2.16, were determined. The calculated MFD's and their overlap values with beams focussed by objective lenses with two different NA's are shown in Table 2.1. Interesting is that contrary to the expectations, a lens with a NA = 0.4 gives a better overlap than an objective lens with NA = 0.85. This is because of the elliptical shape of the fundamental mode in the channel.

Table 2.1: Mode field diameter and overlap values for different channel geometries. The channel width is $2.0\mu\text{m}$ for all measured waveguides and have no cladding. Due to the elliptical shape of the fundamental channel mode and circular Gaussian beam shape, an overlap mismatch is always present.

sample	core height	etch depth	horizontal MFD	vertical MFD	overlap values	
	[μm]	[μm]	[μm] ($1/e^2$)	[μm] ($1/e^2$)	NA = 0.85	NA = 0.4
4186	0.413	0.070	2.36	0.61	46%	66%
4194	0.623	0.100	2.61	0.71	43%	67%

Values for the reflection at the interface due to different refractive indices for air and the material are about 6%, estimated using normal incidence Fresnel reflection:

$$T = 1 - R = \frac{4n_1n_2}{(n_1 + n_2)^2} \quad (2.17)$$

where $n_1 = 1$ for air and $n_2 = 1.66$ for Al₂O₃. This yields a transmission of about 94% at both interfaces for the pump beam.

2.5 Experimental results

Gain has been measured for five different Nd³⁺ concentrations ranging from $1.13 - 2.95 \cdot 10^{20} \text{ cm}^{-3}$ in 1-cm-long channel waveguides. Slab waveguide losses at 1064 nm for these concentrations average to a value of 0.6 dB/cm [22]. After channels have been etched in Al₂O₃, the propagation losses will increase by 0.1 dB/cm to a total propagation loss of $\alpha = 0.7$ dB/cm [12]. This value was subtracted from the measured gain, according to equation 2.15 to yield the internal net gain.

An incident pump power of 185 mW corresponds to 10 – 20 mW of power in the channel, based on overlap calculations and estimated reflections. However, these values have been obtained for the ideal case, assuming a perfect Gaussian input beam, and perfect input and output facets. In reality, the power in the channel will be lower than is calculated here, depending on the input facet quality. The unknown input and output facet quality and consequently the input and output pump-power coupling efficiencies make it very difficult to estimate the real pump power launched into the channel.

The gain shown in Figure 2.5 has been plotted as a function of the Nd³⁺ concentrations in Figure 2.6. The gain in Figure 2.6 is measured at an incident pump power of 185 mW. At this incident pump power all the curves have saturated to a fixed gain value.

For a concentration of $1.13 \cdot 10^{20} \text{ cm}^{-3}$, a 2.0 dB/cm signal gain has been measured. The measured gain then increases to a maximum value of 4.0 dB/cm for a concentration of $1.68 \cdot 10^{20} \text{ cm}^{-3}$. For concentrations higher than $1.68 \cdot 10^{20} \text{ cm}^{-3}$, the measured gain decreases again, probably due to more significant upconversion in the doped material.

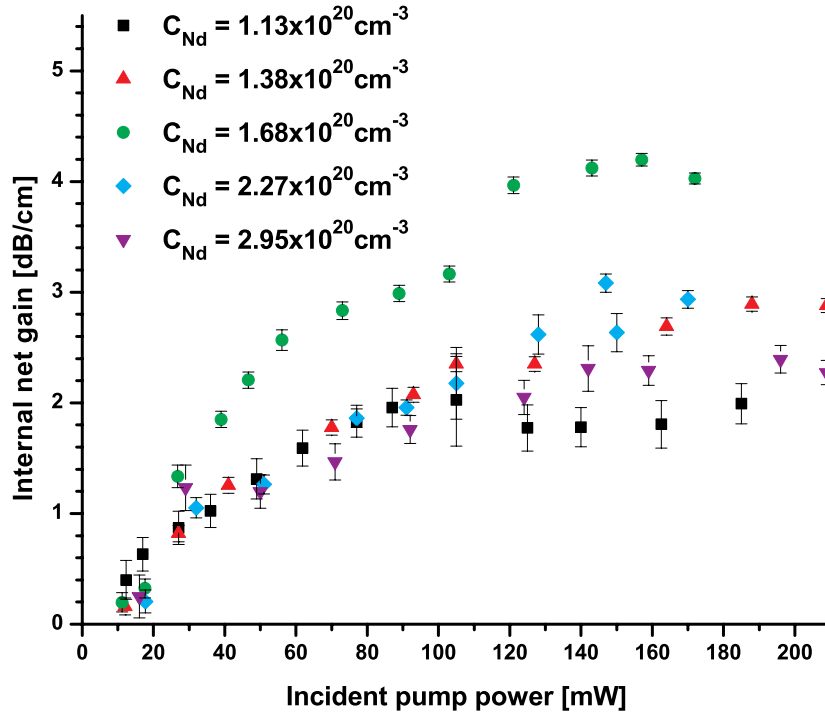


Figure 2.5: Measured gain curves for different Nd dopant concentrations. All measurements were conducted in the small signal gain regime to measure the maximum gain. g increases with increasing pump power until it saturates. The concentration for which the highest gain was measured was $1.68 \cdot 10^{20} \text{ cm}^{-3}$. At this concentration, internal net gain of 4 dB/cm was measured in a 1-cm-long channel.

2.6 Conclusions

Nd^{3+} ions in Al_2O_3 exhibit strong absorption at a wavelength of 800 nm, and strong emission at 1064 nm. Gain at 1064 nm, for different Nd concentrations has been measured in 1-cm-long Nd-doped Al_2O_3 waveguides. A maximum internal net gain of 4.0 dB has been observed for a Nd concentration of $1.68 \cdot 10^{20} \text{ cm}^{-3}$. This gain is competitive with other materials in terms of gain, and it is anticipated that this gain is sufficient for integrated Nd-doped channel amplifiers and lasers. The silicon-compatible Al_2O_3 make these results especially appealing, as integrated devices can be directly patterned in this material [12, 23]. For Nd concentrations larger than $1.68 \cdot 10^{20} \text{ cm}^{-3}$, the measured gain decreases, due to various energy-transfer upconversion processes in the material [17].

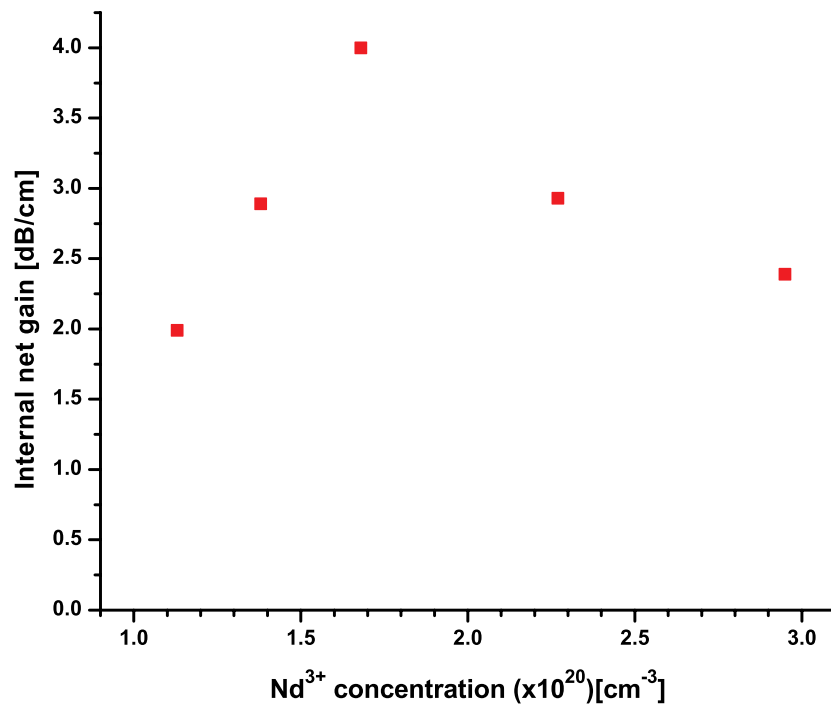


Figure 2.6: Maximum gain versus the Nd dopant concentration. Values were measured at an incident pump power of 185 mW.

Chapter 3

Nd as a laser ion

3.1 Introduction

In the previous chapter optical gain has been observed in Nd-doped Al_2O_3 waveguides at 1064 nm. It has been shown that sufficient gain has been obtained to design integrated Nd-doped amplifiers and lasers in Al_2O_3 . In this chapter simulations will be used to investigate the behavior of Nd-doped Al_2O_3 waveguide lasers, employing a software package to numerically solve the rate equations. This chapter will discuss the various processes that influence laser behavior in terms of rate equations. The simulations will be explained and the results will be discussed.

3.2 Laser theory

3.2.1 Radiative and non-radiative emission

In the previous chapter, optical gain in Nd-doped Al_2O_3 waveguides at 1064 nm has been discussed, which is a results of stimulated emission. There are also other means through which an ion can release its energy and go from a high energy level to a lower energy state. One such a mechanism is spontaneous emission. For spontaneous emission, an ion in a high energy state can release its energy by emitting a photon corresponding to the energy difference between the two energy states. This photon is not the result of another photon triggering the ion to release its energy as is the case for stimulated emission. Another mechanism is non-radiative emission, which is caused by lattice vibrations, absorbing energy of the ion. The energy transfer due to these lattice vibrations are also known as phonon relaxations. The non-radiative and radiative emission can be written as:

$$\frac{dN}{dt} = -\frac{N}{\tau} \quad (3.1)$$

where $1/\tau$ is the combined rate of radiative and non-radiative emissions by:

$$\frac{1}{\tau} = \frac{1}{\tau_{sp}} + \frac{1}{\tau_{nr}} \quad (3.2)$$

where $1/\tau_{sp}$ is the spontaneous emission decay rate and $1/\tau_{nr}$ is the non-radiative decay rate [20].

3.2.2 Secondary processes

Apart from spontaneous, stimulated emission and nonradiative decay due to phonon relaxation, various secondary processes influence the population density of the upper ion energy levels. The main processes are cross-relaxation (CR) and energy-transfer-upconversion. (ETU)

Cross-relaxation is the process during which one ion (a) in an high-energy state transfers its energy to an ion (b) in a low-energy state, resulting in the first ion (a) ending up in a lower energy state while the second ion (b) ends up in a high-energy state.

Energy-transfer-upconversion is the process during which one ion (a) in a high-energy level transfers its energy to a nearby ion (b) in a high-energy level, exciting that ion (b) to an even higher level while the first ion (a) drops to a lower energy level.

3.2.3 Rate equations

Laser operation is governed by a number of equations describing the population of the energy levels: [17, 24]

$$\begin{aligned}
\frac{dN_8}{dt} &= W_3 N_4^2 - \frac{N_8}{\tau_8} \\
\frac{dN_7}{dt} &= W_2 N_4^2 + \frac{N_8}{\tau_8} - \frac{N_7}{\tau_7} \\
\frac{dN_6}{dt} &= W_1 N_4^2 + \frac{N_7}{\tau_7} - \frac{N_6}{\tau_6} \\
\frac{dN_5}{dt} &= R_{05} + \frac{N_6}{\tau_6} - \frac{N_5}{\tau_5} \\
\frac{dN_4}{dt} &= \frac{N_5}{\tau_5} - \frac{N_4}{\tau_4} - 2[W_1 + W_2 + W_3]N_4^2 \\
\frac{dN_3}{dt} &= \beta_{43} \frac{N_4}{\tau_4} - \frac{N_3}{\tau_3} + W_1 N_4^2 \\
\frac{dN_2}{dt} &= \beta_{42} \frac{N_4}{\tau_4} + \frac{N_3}{\tau_3} - \frac{N_2}{\tau_2} + W_2 N_4^2 \\
\frac{dN_1}{dt} &= \beta_{41} \frac{N_4}{\tau_4} + \frac{N_2}{\tau_2} - \frac{N_1}{\tau_1} + W_3 N_4^2 \\
\frac{dN_0}{dt} &= -R_{05} + \beta_{40} \frac{N_4}{\tau_4} + \frac{N_1}{\tau_1}
\end{aligned} \tag{3.3}$$

The β_{4x} terms are the 'branching ratio's'. These account for radiative and nonradiative decay from the 4th level to level x , with $x < 4$. The W terms account for the upconversion process. Since 2 ions are involved, these W 's appear in two levels, hence the factor 2 in dN_4/dt .

Level 4 corresponds to the ${}^4F_{3/2}$ energy level. This is the energy level that is most important to laser behavior, as this is the energy level from which signal photons are generated, through stimulated emission. The population density of level 4 thus determines the stimulated emission rate, discussed in Chapter 2. Figure 2.1 in Chapter 2 shows the energy diagram corresponding to the rate equations above. The upconversion, denoted by W -factors in the rate equation dN_4/dt correspond to the lines tagged with 'UC₁₋₃' in the aforementioned figure. It is assumed that energy levels 3,2 and 1 non-radiatively decay into the next lower-lying level.

Solving the rate equations analytically is nearly an impossible task if these equations are not simplified. The rate equations written above can be simplified to:

$$\begin{aligned}\frac{dN_4}{dt} &= R_{04} - \frac{N_4}{\tau_4} - W_c N_4^2 \\ N_0 &= N_T - N_4\end{aligned}\tag{3.4}$$

where $W_c = W_1 + W_2 + W_3$ is the combined upconversion coefficient. This simplified formula arises from the assumptions that the populations of levels 1 – 3 quickly decay to the ground level 0. Furthermore, levels 5 – 8 exhibit a fast decay to level 4. Any upconversion adding to the population densities in levels 6 – 8 will also rapidly decay back to level 4, removing the need for the factor 2 in front of W_c . Equation 3.4 shows that the combined upconversion parameter W_c acts as an additional 'loss' to the population in level 4, in addition to radiative and nonradiative decay. The upconversion rate depends quadratically on the population density N_4 .

3.2.4 The laser cavity

A basic laser cavity consists of a gain medium and two mirrors. By pumping the gain medium, laser photons are generated and gain will be achieved. Lasing can be achieved through the mirrors, which requires one mirror to be transparent at the pump wavelength. Alternatively, the active gain medium can be pumped from the side, but in integrated optics this is not desirable. The rate equations indicate that the stimulated emission rate depends on the intensity of signal photons. This means that in order to generate more laser photons and to fully exploit the gain exhibited by the active medium, a feedback mechanism is required to increase the amount of laser photons. This feedback mechanism is provided by means of the mirrors. One, or both of the mirrors have to have a reflectivity lower than 100% in order to allow a small percentage of laser photons to escape the cavity. The photons that escape the cavity are the laser photons that we are interested in.

3.2.5 Laser threshold

Due to stimulated emission, laser photons will be generated in the material. Some of these laser photons will again be lost due to absorption or other losses in the cavity. Other losses include scattering losses in the gain material, as well as losses due to the mirrors. In order to get a build-up of laser photons in the cavity, the laser gain must exceed the laser losses. Laser threshold is reached at a certain pump power at which the gain equals the total loss of the cavity.

For the amount of laser photons in the cavity we can write:

$$\phi_2 = \phi_1(1 - L) \exp[(g - \alpha)l]^2 R_1 R_2\tag{3.5}$$

where R_1 and R_2 are the mirror reflectivities. L is the intrinsic cavity loss. l is the active medium length and ϕ represents the photon flux. The coefficients α and g represent the total propagation losses in the active medium and the gain in the active medium, respectively.

When the photon flux after one roundtrip, ϕ_2 , equals the photon flux before one roundtrip, ϕ_1 , the gain equals the losses. Putting $\phi_1 = \phi_2$ in equation 3.5 yields:

$$g_{thr} = \alpha - \log_e [(1 - L)R_1 R_2] / 2l\tag{3.6}$$

where g_{thr} is the gain at threshold.

3.3 Simulation of Nd-doped Al₂O₃ lasers

The set of rate equations 3.3 can be analyzed numerically. [25] We have analyzed a channel waveguide with a cross-section that is comparable to the cross-sections of the waveguides measured later on in this thesis. The simulated channel has a height of 0.3 μm and a width of 1.2 μm . A perfect overlap between pump and signal fundamental modes has been assumed, while in reality it is about 92% for TE polarization and 90% for TM polarization. A channel length of $l = 1.25$ cm is used, which is comparable to the $1/e$ absorption length of the pump intensity for the concentrations used.

Table B.1 in the Appendix shows the concentration-independent parameters, such as cavity parameters, used in the simulations. For both cavity mirrors, a reflectivity of 98% was used in these simulations. A background propagation loss of 0.9 dB/cm was assumed for both pump and signal wavelengths.

The lifetimes of the ${}^4\text{F}_{3/2}$ laser level for different concentrations are given in Table 3.1. These lifetimes were measured by fluorescence intensity decay [26]. The combined upconversion parameter W_c is also strongly concentration-dependent, but at present no accurate value for the upconversion parameter at different Nd concentrations in Al₂O₃ is known. A value for the upconversion $W_c = 1.7 \cdot 10^{-16}$ cm³s⁻¹ was used as a starting point in these simulations. This is the combined upconversion value measured for Nd:YLF, by Guyot et al. [27]

Table 3.1: Concentration dependent parameters for the two different Nd dopant concentrations used in the simulations.

Nd concentration	${}^4\text{F}_{3/2}$ lifetime
[cm ⁻³]	[μs]
$1.13 \cdot 10^{20}$	337
$1.68 \cdot 10^{20}$	309

3.4 Simulation results

To investigate the effect of the upconversion rate on the pump absorption and signal output, we have numerically analyzed the rate equations of equation 3.3 with two different values for the combined upconversion coefficient W_c [25]. Values used for W_c are $W_c = 0$, to study the behavior of the laser with no upconversion present, and $W_c = 1.7 \cdot 10^{-16}$ cm³s⁻¹. Two different values for the Nd concentrations were also analyzed. Figures 3.1a and b show the remaining pump power in the active medium and the absorption coefficient α as a function of propagation distance in the active medium, respectively.

From Figure 3.1 it is clear that upconversion has little or no effect on the pump absorption. The pump power in the active medium for the two different Nd concentrations show perfect overlap between the curves, regardless of the value for the combined upconversion W_c . The absorption coefficient α is therefore also invariant for different upconversion values as can be

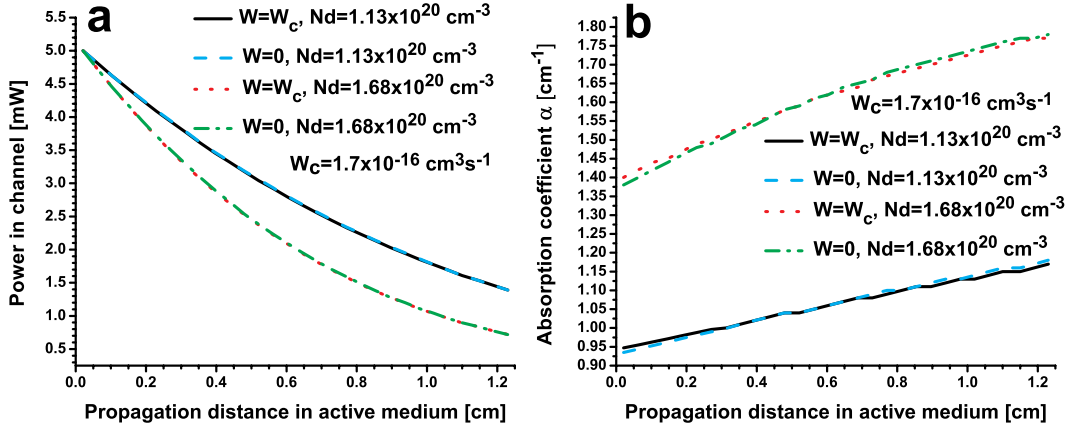


Figure 3.1: The remaining pump power in the channel as a function of propagation distance for two different Nd concentrations. Figure (b) shows the pump absorption coefficient α as a function of the propagation distance in the active medium.

seen in Figure 3.1b. The increase of α over propagation distance can be explained by an increase of ions occupying the ground level, leading to a higher absorption rate. Figure 3.2 shows the signal power at 1064 nm as a function of the pump power in the channel at 800 nm. The same values for the Nd concentration and upconversion W_c as in Figure 3.1 were used. The results show that the slope efficiencies are not significantly influenced by different upconversion rates. The slope efficiency is 2.8% for a Nd concentration of $1.13 \cdot 10^{20} \text{ cm}^{-3}$. For a Nd concentration of $1.68 \cdot 10^{20} \text{ cm}^{-3}$ the slope efficiency is 3.6%.

The threshold pump power in case no upconversion is present, is less than 0.5 mW for both Nd concentrations. When upconversion is present in the active medium, the threshold pump power increases to a value of ± 1 mW. The reason for the increase in threshold pump power lies in the fact that the pump rate into the ${}^4F_{3/2}$ level must first overcome the losses due to (non-)radiative emission and upconversion. This can be seen in equation 3.4.

Figure 3.3 shows the signal power as a function of pump power for different mirror reflectivities. The concentration is held fixed at $\text{Nd} = 1.68 \cdot 10^{20} \text{ cm}^{-3}$, and the combined upconversion $W_c = 1.7 \cdot 10^{-16} \text{ cm}^3\text{s}^{-1}$. For a mirror reflectivity of 99%, the threshold pump power is well below 1 mW, but the slope efficiency is only 1.86%. For a mirror reflectivity of 88%, the slope efficiency has increased to 15.2%, at the cost of a higher threshold pump power of about 1.8 mW.

These results show that for the channel geometries used in this thesis, the mirror reflectivities can be lower than 90%, provided the pump power that can be launched into the channel exceeds several mW's. When one mirror has a reflectivity of 100%, the outcoupling mirror can have a reflectivity well below 80%.

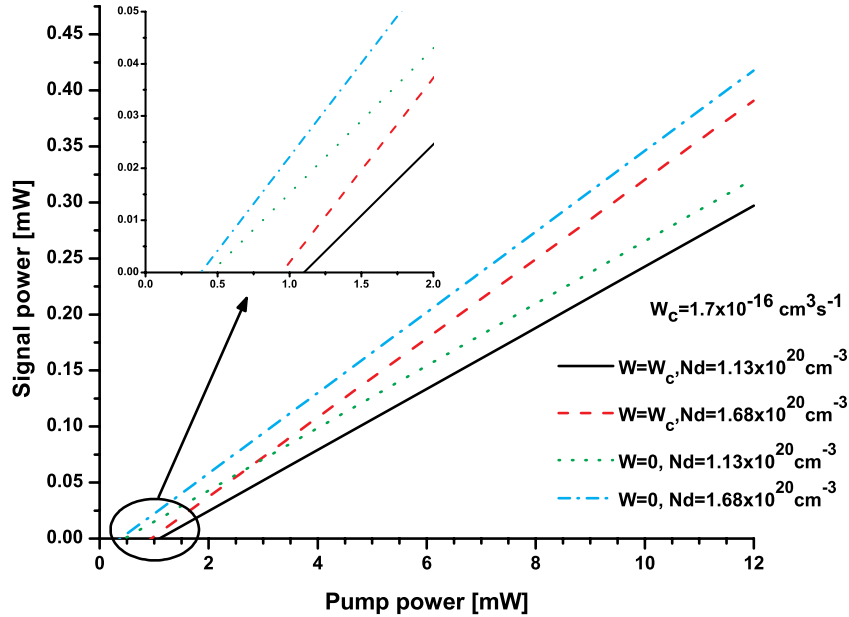


Figure 3.2: Calculated laser signal power at 1064 nm as a function of pump power at 800 nm, for two different Nd concentrations and two different combined upconversion values W_c . The highest concentration shows the highest slope efficiency. The inset shows a threshold pump power of less than 0.5 mW for both concentrations when no upconversion is present, but increases to ± 1 mW when upconversion is present.

3.5 Conclusions

The laser properties of Nd-doped Al_2O_3 channel waveguides have been investigated by simulation based on rate equations.

Upconversion rates have a negligible effect on the slope efficiency for the simulated channels in this chapter. Only the threshold pump power is increased at higher upconversion rates. The absorption coefficient is hence also invariant to a changing upconversion rate. The absorption coefficient increases for increasing ground-level population. This means that the absorption coefficient is lowest at the beginning of the channel, where a high percentage of ions occupy a higher energy level.

Different mirror reflectivities have been investigated by simulations. The results show that a mirror reflectivity of 88% results in a threshold pump power of 1.8 mW and a slope efficiency of 15.2%, at a Nd concentration of $1.68 \cdot 10^{20} \text{ cm}^{-3}$.

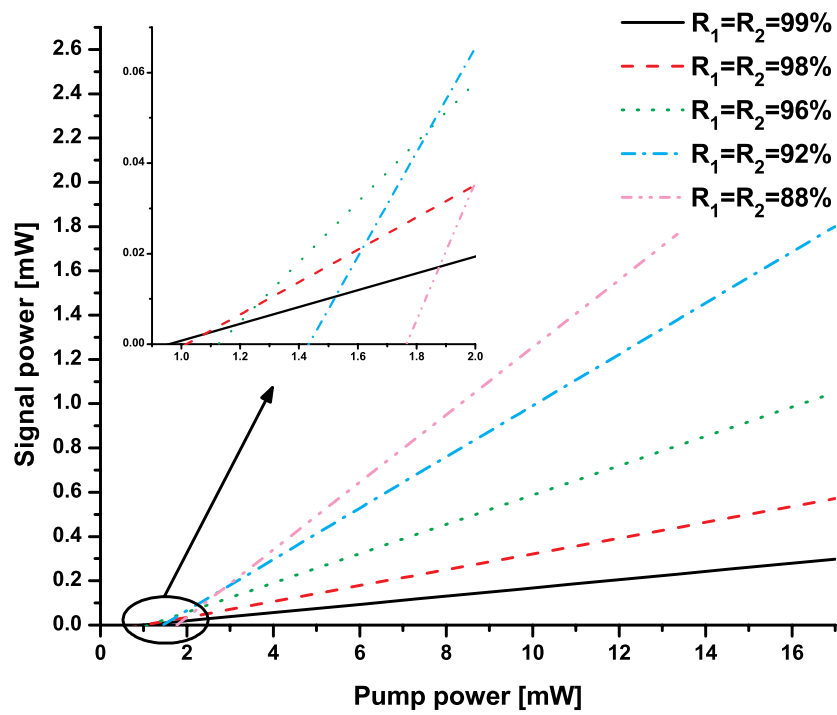


Figure 3.3: Calculated laser signal power as a function of pump power for $Nd = 1.68 \cdot 10^{20} \text{ cm}^{-3}$, and $W_c = 1.7 \cdot 10^{-16} \text{ cm}^3\text{s}^{-1}$. Different mirror reflectivities were used to study the threshold and slope efficiency.

Chapter 4

Waveguides and couplers

4.1 Introduction

In the previous chapter we have seen that an integrated Nd-based laser is feasible, based on simulations. In order to design such a laser, information about the modes of the pump and laser wavelength must be obtained and ways to reflect light in the waveguides. Since a Sagnac mirror will be used for reflecting laser light, couplers will have to be studied by simulation and experiment, as a Sagnac mirror contains these directional couplers. This chapter will begin with explaining waveguide theory. The effect of the channel geometry on the effective refractive index of a guided mode will be discussed. This effective refractive index determines the confinement of a mode within a waveguide channel. After the basics of a single channel have been discussed, we will investigate Nd:Al₂O₃ waveguide couplers. The influence of changing channel geometry on the coupling strength of a directional coupler will be investigated. Two types of directional coupler devices were compared using simulations, to investigate their sensitivity to changes in waveguide geometry. Finally, experimental results of measured directional coupler devices will be discussed and compared to the results from simulations.

4.2 Theory

4.2.1 Waveguides

Integrated optics differs from free-space optics in the way that in integrated optics light is confined within an optically dense medium with respect to its surrounding material. A requirement for light to be confined is that the refractive index of the material through which light propagates has a higher refractive index than its surrounding material. The high refractive index material is commonly referred to as 'core', while its surrounding material is referred to as 'cladding'. In integrated optics, where light is guided across a chip, a high refractive index core waveguide is deposited onto a substrate, or alternatively 'written' into a high refractive index material. The surrounding cladding material can be any material, even air, as long as this material has a lower refractive index than the core material. In this thesis, our research is focussed on Al₂O₃ that is grown onto a substrate material, SiO₂. The cladding material is either air or SiO₂.

Light within the core will be confined as long as the total internal reflection condition is

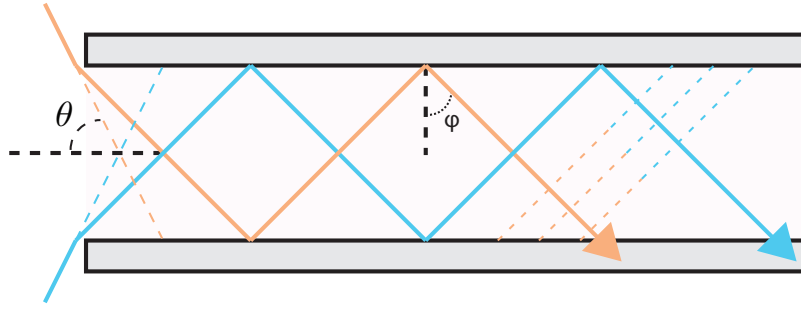


Figure 4.1: Ray picture for a slab waveguide. Light is coupled into a channel from the left, at an angle $\theta < \theta_{\max}$. Light is confined and guided by total internal reflections at the core-substrate and core-cladding interfaces. Phase-consistency must be maintained throughout the channel for a mode to be able to propagate. The dashed lines represent the phase-fronts which are in phase with one another in this particular picture.

fulfilled. The angle for total internal reflection solely depends on the relative refractive indices of the core and cladding materials. For a core having a much higher refractive index than its surrounding material we say that the core has a high index contrast and as a result light traversing the channel is strongly confined. The condition for total internal reflection is given by $\phi_c = \sin^{-1}(n_1/n_0)$ and can be re-written into a function for the maximum acceptance angle for coupling into the channel from outside: [28]

$$\theta \leq \sin^{-1} \sqrt{n_1^2 - n_0^2} \equiv \theta_{\max} \quad (4.1)$$

In the equation defined above, $\sin \theta_{\max}$ is also known as the numerical aperture, NA, of the channel. Our waveguides based on Al_2O_3 onto SiO_2 exhibit a rather large index contrast resulting in a numerical aperture $\text{NA} = 0.81$.

Apart from the requirement that light may only propagate through the waveguide when its propagating angle is less than the maximum acceptance angle, a second condition defines whether or not light can propagate. This second requirement, called the resonance condition, is that light cannot propagate when its phase-fronts cancel out one another while traversing the channel. Taking this requirement into account yields a discrete number of 'modes' that can propagate through the channel. While the previously discussed critical angle does not depend on the waveguide geometry but only on relative refractive indices, the number of allowed modes does depend on waveguide geometry. For a symmetric waveguide, meaning the core is surrounded by a uniform cladding refractive index, at least one mode is supported regardless of the core dimension. Waveguides having a cladding with a different refractive index than the substrate are called asymmetric waveguides. For these asymmetric waveguides, a minimum core cross-section is required in order to guide modes. The waveguides investigated in this research are all asymmetric waveguides.

The resonance condition for a slab waveguide can be expressed by:

$$2k_0 n_1 h \cos \phi - 2\Phi_c - 2\Phi_s = 2\pi\nu \quad (4.2)$$

where $k_0 = 2\pi/\lambda_0$, and ν is an integer denoting the mode index, where $\nu = 0$ is the fundamental mode. n_1 is the core refractive index and h its height. $-2\Phi_c$ and $-2\Phi_s$ are the Goos-Hänchen phase-shifts at the core-cladding and core-substrate interfaces, respectively.

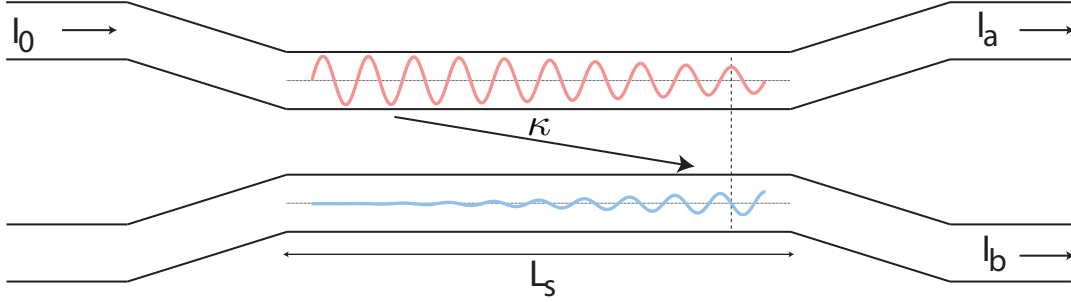


Figure 4.2: Diagram of a directional coupler structure. Two waveguides are brought together causing overlap of their respective evanescent fields which results in power transfer between the waveguides. In case power is present in both channels, the relative phase determines the direction in which power flows: the 'donating' field leads by relative phase-shift of $\frac{\pi}{2}$. In the figure, an initial field with intensity I_0 propagates through the upper-left channel. After propagation through the narrow, straight section of physical length L_s , the lower-right channel contains an intensity $I_b = \kappa I_0$. The coupling coefficient κ depends strongest on the physical length L_s of the coupler section where the waveguides are nearest one another. The bend sections contribute an effective length L_b in addition to this.

The Goos-Hänchen phase-shift will not be discussed here. See a discussion by H. Kogelnik [29] on the Goos-Hänchen shift.

Each of the supported, discrete modes have their own propagation index, denoted by:

$$\beta = k_0 n_1 \sin \phi = k_0 N_{\text{eff}} \quad (4.3)$$

where N_{eff} is called the effective mode index. This parameter will be used extensively throughout in this report, as this parameter is often calculated in simulations.

4.2.2 Directional coupler

When two waveguides are brought in close proximity, light traversing one channel may excite a mode inside the other channel by the evanescent field extending into this waveguide, Figure 4.2. The coupling strength depends on the magnitude of the evanescent field of the mode in one channel (a) inside the other channel (b). The coupling strength is therefore a function of the mode confinement and the separation between the channels; waveguides having strongly confined modes but having a small separation distance may have just as strong coupling as two waveguides having weak confinement and a large separation distance. Once two waveguides are 'connected' through their respective evanescent fields, light will start flowing between the two waveguides where the relative phase of the respective field determines the direction of the energy flow. A field in one waveguide will act as the 'driving field', whereas the field in the adjacent waveguide will be the 'driven field'. The driving field is leading with a $\frac{\pi}{2}$ phase with respect to the driven field. A better way of putting this is saying that the driven field is trailing behind by a $-\frac{\pi}{2}$ relative phase. This implies that coupling of light between two channels always introduces a -90° phase shift. It also means that the driving field will couple 100% into the adjacent waveguide even if the field intensity of the driven field exceeds the driving field intensity. Once 100% of the field intensity of the driving field has coupled into the adjacent waveguide, the fields switch roles. The former driven field will now become the

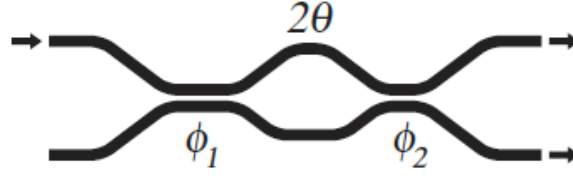


Figure 4.3: The layout of a directional coupler employing a Mach-Zehnder structure. [30]

driving field and vice versa, meaning that light can now couple back into the first waveguide. The coupling strength, which depends on channel separation as explained above, determines the distance over which 100% of the field intensity couples into the other waveguide in a single pass. This distance, also called coupling length, is denoted by L_c .

The coupling coefficient of a coupler is given by:

$$\kappa = \sin^2 \phi \quad (4.4)$$

where $\phi = \pi L/2L_c$. Here, L is the length of the coupler and L_c is the previously mentioned coupling length required for 100% power coupling from one waveguide to the other. When studied in more detail, $L = L_s + L_b$ where L_s is the physical length of the straight section of the coupler and L_b is an effective length. This effective length L_b originates from coupling in the two coupler bend sections since light already begins to couple just prior to entering the coupler straight section.

Consider a mode with intensity I_0 , introduced in the upper channel in Figure 4.2. The field intensity in the two arms after having traversed the coupler is now:

$$\begin{aligned} I_a &= (1 - \kappa)I_0 \\ I_b &= \kappa I_0 \end{aligned}$$

The coupling length L_c is given by:

$$L_c = \frac{\lambda}{2\Delta N_{\text{eff}}} \quad (4.5)$$

where ΔN_{eff} is the difference between the effective indices of the symmetric and antisymmetric modes in two adjacent channels that make up the coupler.

4.2.3 Mach-Zehnder coupler (or balanced coupler)

A directional coupler as discussed in the previous section is rather simple to analyze mathematically and to realize on a chip. However, it is reported to be extremely sensitive to waveguide geometry errors introduced during the fabrication process. A more sophisticated device called Mach-Zehnder, or balanced, coupler consists of two cascaded directional couplers, between which a phase-shift is introduced in one of the waveguides. Such a Mach-Zehnder coupler is shown in Figure 4.3. The purpose of this is to negate the effect of development errors on the performance of the coupler device. The basic idea is that waveguide geometry errors introduced during device fabrication causing stronger coupling in the first directional



Figure 4.4: Coupler geometry as generated by FieldDesigner. Based on this geometry, the effective propagation modal indices are calculated from the entered refractive indices of the different materials and waveguide dimensions.

coupler, for example, is cancelled out by weaker coupling in the second and third section of the device. The coupling coefficient of the balanced coupler is given by:

$$\kappa_{mz} = \cos^2 \theta \sin^2(\phi_1 + \phi_2) + \sin^2 \theta \sin^2(\phi_1 - \phi_2) \quad (4.6)$$

Here, ϕ_1 and ϕ_2 describe the total integrated coupling of the two constituent directional couplers, again given by $\phi_n = \pi L_n / 2L_c$ and 2θ is the phase-shift introduced by unequal armlengths separating the two directional couplers.

In order to design the balanced coupler as a fabrication-error insensitive device, the subsequent couplers and their respective phase shift must be chosen as follows: [30, 31]

$$\begin{aligned} \phi_1 &= \frac{3\pi}{8} \left(1 + \frac{1}{N}\right), \phi_2 = \frac{3\pi}{8} \left(1 - \frac{1}{N}\right) \\ \cos^2 \theta &= \sin \left(\frac{3\pi}{2N}\right) \left[N + \sin \left(\frac{3\pi}{2N}\right)\right]^{-1} \end{aligned} \quad (4.7)$$

Here, N is a dimensionless factor governing the power splitting, or coupling, behavior of the balanced coupler by:

$$\kappa_0 = \frac{1}{4} \sin \left(\frac{3\pi}{N}\right) \left[N + \sin \left(\frac{3\pi}{2N}\right)\right]^{-1} \quad (4.8)$$

The purpose of eqn. 4.8 is to select a desired coupling coefficient κ_0 for the balanced coupler, deduce N and use this N to set the parameters ϕ_1 , ϕ_2 and 2θ . In the special case of a $\kappa_0 = 0.5$ or 3 dB balanced coupler, this results in $\phi_1 = \frac{\pi}{2}$, $\phi_2 = \frac{\pi}{4}$, and $\theta = \frac{\pi}{3}$. In a later section we will see that this 3 dB balanced coupler is the type of coupler we are most interested in.

4.3 Simulations

4.3.1 Simulation procedure and software

The geometry of a waveguide and its dimensions have a large influence on the propagation behavior of waveguide mode inside. The number of modes, their confinement within the channel and propagation losses are for a large part determined by the channel geometry. Therefore, numerous commercial simulation software packages have been developed to study the effect of channel dimensions and geometry on its propagation properties. A software package called FieldDesigner has been used to calculate the number of modes and their

Table 4.1: The default set of parameters with which coupler simulations were carried out.

Layer	Material	Thickness [μm]	Width [μm]	n_{pump}	n_{signal}
Substrate	SiO ₂ (thermal)	8	40	1.455	1.453
Slab	Al ₂ O ₃	0	40	1.660	1.658
Core	Al ₂ O ₃	0.3	1.2	1.660	1.658
Cladding	SiO ₂ (PECVD)	5	40	1.449	1.447

effective refractive index, based on the defined cross-section of a waveguide. Couplers were simulated using a geometry as is shown in Figure 4.4. Symmetric and antisymmetric modes were calculated to determine the coupling length L_c , using equation 4.5.

The refractive indices of the materials used have to be provided for the software to calculate the channel modes. A list of material properties such as were used in our simulations is provided in Table 4.1. This table contains the refractive indices of the channel and layers as well as their thickness. The dimension of the core is also specified.

4.3.2 Waveguide mode analysis and calculations

In order to find the number of modes for a straight channel a single waveguide was defined in FieldDesigner as discussed above. The number of modes for signal, $\lambda = 800$ nm, and pump wavelength, $\lambda = 1064$ nm, were calculated for both TE and TM polarization. Figure 4.5 shows the effective indices for a channel height of $0.3 \mu\text{m}$ and varied width, such as is the investigated channel geometry in this research. At these channel dimensions, only fundamental modes at signal wavelength are supported, while light at pump wavelength is multimode. The simulation indicates that modes at TE polarization yields a stronger effective refractive index N_{eff} than modes at TM polarization, and are therefore stronger confined. A difference in refractive index for pump wave and signal wavelength is also visible: the effective refractive index for signal wavelength is lower than for pump wavelength. As a result, pump light will experience a stronger confinement than signal light.

4.3.3 Couplers

The geometry shown in Figure 4.4 was used to calculate the coupling length L_c according to equation 4.5, both for TE and TM polarizations. In general, coupling efficiency for modes at TM polarization was found to be stronger than for TE polarization due to the weaker mode confinement and therefore further extension of the evanescent field into the adjacent channel. The influence of the gap between two waveguides in the coupler region on the coupling strength has been studied, along with the effect of different channel dimensions. The results shown in Figure 4.6 indicate that a smaller channel separation leads to a smaller coupling length L_c , which means stronger coupling as the length over which 100% power couples into the other waveguide is decreased. A similar increase in coupling strength has been observed when a channel's height is decreased. This can be explained by a smaller

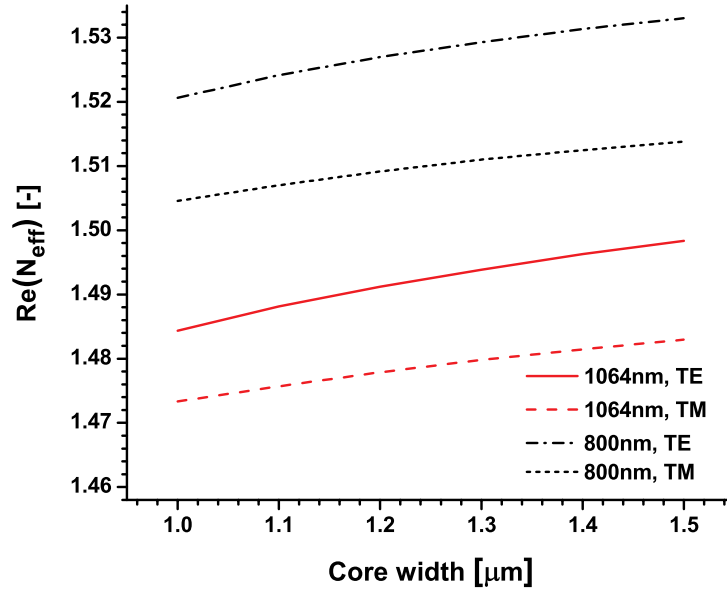


Figure 4.5: Evolution of fundamental mode effective indices ($N_{\text{eff}0}$) vs. core width, at a fixed core height of $0.3 \mu\text{m}$. Effective indices for pump and signal wavelength, $\lambda = 800 \text{ nm}$ and $\lambda = 1064 \text{ nm}$ respectively, are shown for both TE and TM polarization. TE modes show a higher N_{eff} and are therefore stronger confined than their TM counterparts. The effective refractive index at pump wavelength is higher than for signal wavelength. Therefore, pump modes are stronger confined than modes at signal wavelength, regardless of the polarization.

effective index and consequently a weaker confinement for decreasing channel height.

The previous simulations have shown that the slightest deviation in core height, core width or gap size between two coupler waveguides has a drastic effect on the coupling length L_c , caused by a stronger evanescent field overlap from the adjacent channel. During the fabrication process unavoidable deviations from the original design will be introduced requiring the designer to anticipate to this. Therefore, the impact of varied coupling length L_c on the coupling coefficient κ has been studied. Figure 4.7 shows a plot of the impact of a changing coupling length L_c on the coupling coefficient κ .

Two coupler devices were studied. One is the simplest directional coupler, having only one coupling region, and the other is the Mach-Zehnder coupler device. Both coupler devices were simulated to be 3 dB couplers. For the single directional coupler device, Figure 4.7 shows a monotonic decrease for the coupling coefficient κ as the coupling length increases. About the $\kappa = 0.5$ pivot, the single directional coupler experiences a $\pm 20\%$ variation, for a $\pm 10\%$ variation in coupling length L_c . The coupling coefficient of the Mach-Zehnder device remains almost constant across this variation of L_c . Beyond the 10% variation mark, the Mach-Zehnder coupling behavior begins to deviate as well, but not nearly as strong as it is the case for the single directional coupler.

Invariant coupling behavior for the Mach-Zehnder device may be achieved through changing the phase shift 2θ . This enhances the coupling performance with respect to the desired

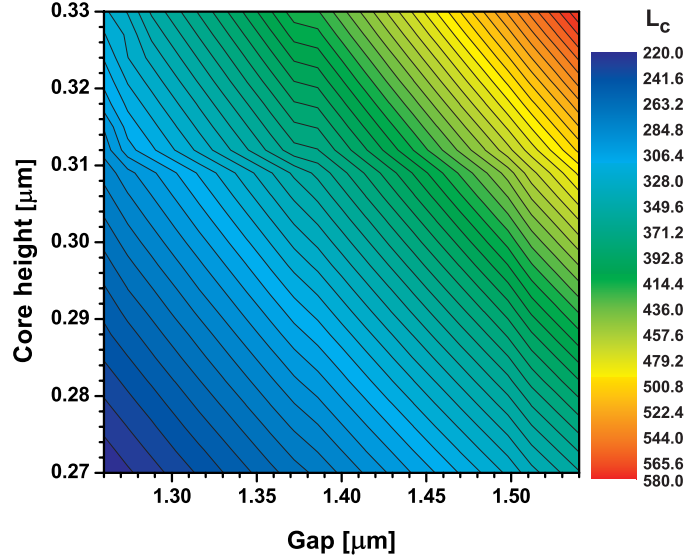


Figure 4.6: Calculated coupling length L_c [μm] as a function of the gap between two waveguides and the channel height. The channel width was held fixed at a value of $1.22 \mu\text{m}$. The couplers that we study in this report have a designed gap of $1.5 \mu\text{m}$. Waveguide properties have been given in Table 4.1. The color plot shows that a narrower gap between the waveguides results in a smaller L_c , thus meaning stronger coupling. A decreased channel height also causes stronger coupling due to weaker confinement of the modal field.

coupling coefficient for larger deviations in L_c , at the cost of less precise coupling behavior when L_c is close to L_{c0} . The effect of changing this phase shift is also shown in the figure. For an increasing phase shift beyond 2θ , the Mach-Zehnder coupler will increasingly mimic a single directional coupler as the single coupler shown in the figure. For a phase shift less than 2θ , the coupling coefficient will fluctuate about the desired value for the coupling coefficient.

4.4 Experimental setup

4.4.1 Coupler measurements

Coupler measurements were carried out using a diode-pumped Nd:YAG laser at 1064 nm. (CrystaLaser IRCL-2W-1064) Light from this linearly polarized source was coupled into a Thorlabs SM600 fiber through a lens with a numerical aperture of 0.25. Light from this fiber was coupled in a polarization retaining PM-500 fiber (Thorlabs) by a fiber-to-fiber linear polarizer (OZ Optics) designed for this wavelength. A polarization rotator was used to match the polarization angle of the linear polarizer and hence to the elliptical PM-500 fiber core. The PM-500 fiber was used to couple light directly into a waveguide coupler, selecting either TE or TM polarization by simply rotating the exit fiber connector with respect to the channel. Afterward, the light was coupled out from the channel by a $9 \mu\text{m}$ fiber, (Thorlabs) and

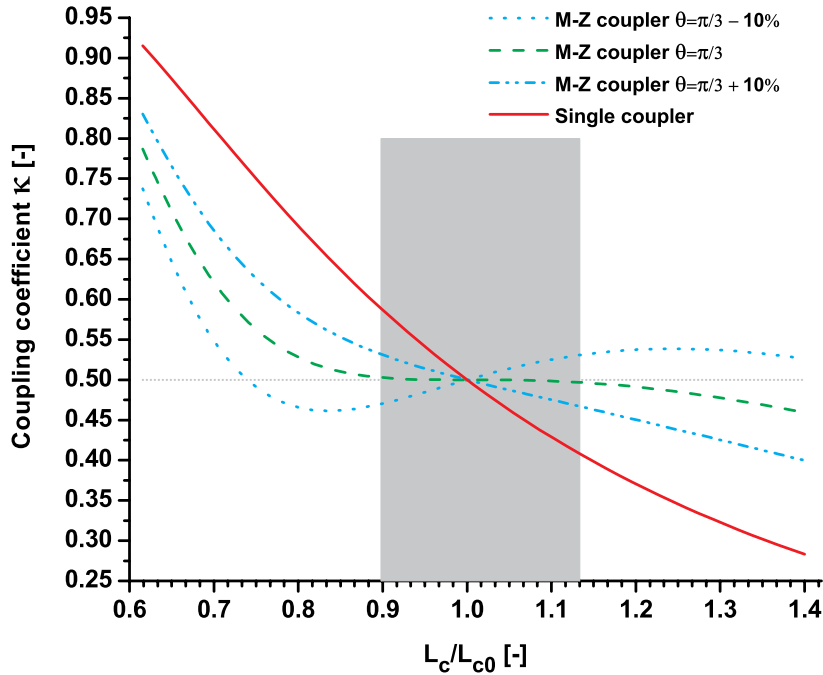


Figure 4.7: Plot of the coupling coefficient κ as a function of coupling length L_c , for a single directional coupler and for a cascaded, balanced (Mach-Zehnder) coupler. Both devices were designed for a 3 dB or $\kappa = 0.5$ power splitting ratio when $L_c = L_{c0}$. Any deviation in coupler geometry and/or dimensions will cause L_c to deviate from L_{c0} . The Mach-Zehnder device was parametrized following design rules of equations 4.7. A $\pm 10\%$ deviation in L_c from L_{c0} results in a $\pm 20\%$ deviation in coupling coefficient κ for the single directional coupler, while the Mach-Zehnder coupler still behaves as a near-perfect 3 dB coupler despite this variation. The shaded area represents the range over which the Mach-Zehnder coupler remains a perfect 3 dB coupler. Two additional lines show the effect of varied phase-shift 2θ separating the two directional couplers in the Mach-Zehnder coupler device.

collected into a HP 8153A detector. The fiber-to-waveguide coupling has been optimized by auto-adjusted micromechanical stages. (Newport)

The PI:Oxide mask contains a number of couplers designed for Nd:Al₂O₃ waveguides, on which 16 couplers are included. The physical length L_s of the couplers ranges from 0 to 750 μm . The thickness of the Al₂O₃ layer for our specifications is 300 nm. The channel width is 1.2 μm and the coupler sections have a minimum channel separation of 1.5 μm . The position of the couplers on the wafers is right at the edge, so deviations in layer thickness is expected.

4.4.2 SEM imaging

SEM images of coupler cross-sections have been taken of cleaved samples using a high resolution SEM microscope. (FEI NovaLab600) Samples were cleaved after being scratched with a diamond-tipped pen. To improve SEM contrast, the cleaved sample was etched for 3 minutes in Al-etch, (MERCK 115435.2500) at 55 $^{\circ}\text{C}$, removing several tens of nanometers of the Al₂O₃

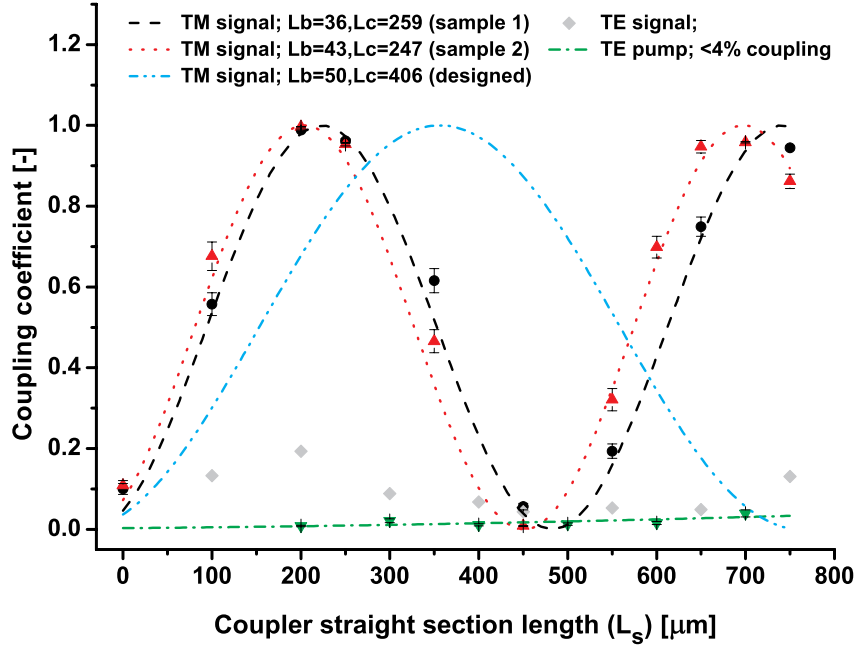


Figure 4.8: Coupling coefficients as a function of physical coupler length L_s , as measured on two different samples for TM polarization. (black,red) The measured values were fitted, which yields coupling lengths $L_c = 259 \mu\text{m}$ and $L_c = 247 \mu\text{m}$ for the two measured samples, respectively, equalling a variation of less than 5% between the two samples. This value differs from the expected, or designed, value of $L_c = 406 \mu\text{m}$ by about 38%. The channels were also measured at TE polarization, and no clear coupler trend could be distinguished. Coupling at pump wavelength was measured to be less than 4%. The reason for the coupling coefficient having a value greater than 0 at $L_s = 0$ originates from the fact that the bend sections of the couplers contribute an effective length L_b to the physical coupler length.

channels while leaving the substrate and cladding untouched. No conductive layer was sputtered onto the sample, as the SEM contrast proved to be sufficient, even for these strongly insulating samples.

4.5 Results

4.5.1 Coupler measurements

Power splitting ratios of a set of couplers with a physical length ranging from 0 – 750 μm were measured and the results are shown in Figure 4.8. The measured splitting ratios were fitted to equation 4.4 and from this, coupling lengths of $L_c = 259 \mu\text{m}$ and $L_c = 247 \mu\text{m}$ were found for two different samples, respectively. Measurements were performed at both TE and TM polarization, but a clear coupling curve could only be discerned for TM polarization. Comparing the measured coupling lengths L_c with the theoretically predicted coupling length $L_c = 406 \mu\text{m}$, based on the designed waveguide geometry, reveals a deviation of 38%. This is

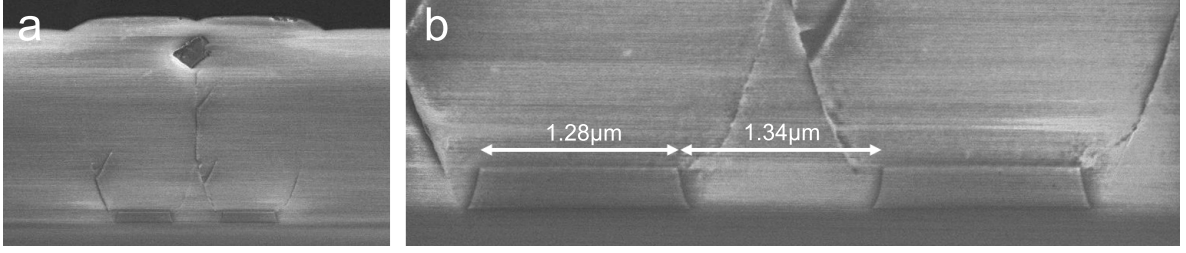


Figure 4.9: SEM close-up of the middle section of a directional coupler with a physical length $L_s = 750 \mu\text{m}$. A sample containing a series of coupler devices was cleaved with scrutiny, assuring the cleave passed through the middle section of the coupler at which point the channel’s gap is at its narrowest. Figure (a) shows an overview of the cross-section, with the channels and the full cladding. Figure (b) shows a zoom-in onto the channels, allowing measurement of the channel dimensions and gap. This particular picture shows a channel width of $1.28 \mu\text{m}$ as compared to a designed channel width of $1.2 \mu\text{m}$ and a gap width of $1.34 \mu\text{m}$, as compared to a designed gap width of $1.5 \mu\text{m}$. This explains the deviation in measured coupling length.

an indication that the fabricated channels have a different geometry than designed.

Apart from coupling behavior at signal wavelength, we are also interested in coupling behavior at pump wavelength. The channels were therefore also investigated at pump wavelength, at TE and TM polarization. For both polarizations, the coupled pump power was found to be less than 4%, which agrees with the theory that pump light will couple much weaker due to stronger confinement.

4.5.2 Coupler SEM analysis

Due to the measured difference in coupling length L_c of the directional couplers, SEM images, Figure 4.9, have been taken of the coupler cross-sections to analyze whether these deviations had their origin in physical deviations from designed channel and coupler geometry. To do this, a sample with fabricated coupler structures was carefully cleaved to ensure the cleave passed through the center coupler section at which point the waveguides have the smallest separation. The geometry of several couplers with a physical coupling length of $600 \leq L_s \leq 750 \mu\text{m}$ was measured. The results of these measurements are given below, in Table 4.2.

Overall, the measured geometry values differ from the geometry for which the couplers

Table 4.2: Geometry parameters deduced from SEM images of cross-sections of the couplers. The upper values in the table result from rough measurements on an overview of the coupler as a whole. More accurate values have been obtained after zooming in. After zooming in, the measured geometry was smaller, but probably more accurate. These zoomed-in values are the lower values in the table and were taken as ‘expected’ values in the table.

	600 coupler	650 coupler	750 coupler	expected	designed
gap [μm]	1.35	1.28-1.36	1.26-1.35	1.28	1.50
channel width [μm]	1.21-1.29	1.27-1.29	-	1.22	1.20
channel height [μm]	0.24 - 0.26	0.25-0.27	0.25-0.26	0.28	0.30

were designed. This explains the difference between the results from measurements and simulations. Plugging the 'expected' values in Table 4.2 into a simulation to calculate a new coupling length at TM polarization, yields a coupling length $L_c = 243 \mu\text{m}$, which agrees reasonably well with previously measured values of $247 \leq L_c \leq 259 \mu\text{m}$.

4.6 Conclusions

The number of modes in Al_2O_3 waveguides has been studied. The results from simulations show that the waveguide only supports single mode at signal wavelength, at 1064 nm. For pump wavelength, at 800 nm, the waveguide is multimode. Due to the high index contrast of the Al_2O_3 material, channel dimensions are tiny in order to get single mode channels at signal wavelength. The high index contrast also yields a high numerical aperture of $\text{NA} = 0.81$.

Influence of the channel geometry on coupler performance has been studied. A deviation of 1% in channel geometry results in tens of micrometer shifts in coupling length L_c , which is a significant percentage of the coupling length of the measured devices.

The coupling length of two types of couplers has been investigated by simulation. Single directional couplers show a strong sensitivity of coupling coefficient κ to a change in coupling length L_c . A shift of $\pm 10\%$ easily results in a $\pm 20\%$ change in coupling coefficient κ . Mach-Zehnder couplers, or balanced couplers, however, are nearly insensitive to variations in coupling lengths L_c and keep a stable coupling coefficient κ even beyond $\pm 10\%$ variations in coupling length.

The coupling coefficient κ has been measured over a full range of couplers with a physical length $0 \leq L_s \leq 750 \mu\text{m}$. The performance of these couplers has been compared to the simulated performance of the couplers based on designed coupler geometry. A deviation of 38% has been observed.

High-resolution SEM images of the cross-section of coupler devices have been taken. The results show a deviation of 15% in the gap between the two waveguides, which explains the strong deviation in measured coupling coefficient compared to the simulated coupling coefficient.

Chapter 5

Integrated optical reflectors for waveguide lasers

5.1 Introduction

Optical reflectors are necessary to provide feedback in a laser: photons at laser wavelength will reflect back and forth between the mirrors, while only a small fraction escapes. This chapter discusses two types of mirrors: passive mirrors, reflecting all light, and Sagnac mirrors that are tunable by design. In the previous chapter, couplers have been studied by simulations and by experiment. In this chapter we will study the effect of these couplers on the Sagnac mirror reflectivity. Bent waveguides will also be discussed in this chapter, as both the passive mirrors and the Sagnac mirrors contain bent waveguide sections.

5.2 Theory

5.2.1 Bend losses

The effective index n of a material consists of real and complex parts, $n = n' - in''$, where its real part n' accounts for the refraction of a wave due to its changing of the phase velocity $v = c/n'$ and its complex part n'' is responsible for absorption. The effective index N_{eff} and corresponding propagation constant β given in the previous chapter thus also consist of real and complex parts:

$$\begin{aligned} N_{\text{eff}} &= N'_{\text{eff}} - iN''_{\text{eff}} \\ \beta &= \beta' - i\beta'' \end{aligned}$$

As a mode propagates through a waveguide, the mode is subject to losses due to absorption. The expression for a mode traversing a channel is:

$$E(z, t) = E_0 e^{\text{Im}(\beta)z} e^{i[\omega t - \text{Re}(\beta)z]}$$

Here, $e^{\text{Im}(\beta)z}$ is the term responsible for the absorption. Writing this term in a form for the loss in dB/cm gives:

$$\text{Loss}[\text{dB/cm}] = 10 \log_{10} \left[e^{-2|\text{Im}(\beta)|0.01} \right] \quad (5.1)$$

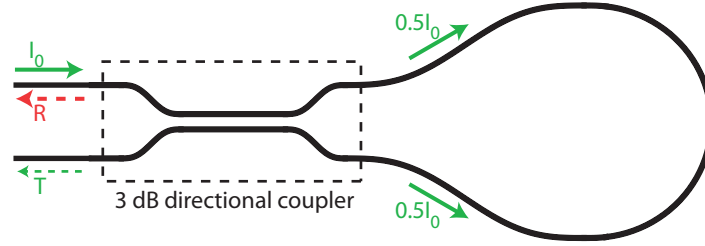


Figure 5.1: Diagram of a Sagnac mirror. Light is fed into the upper channel. The coupler in combination with the loop acts as a mirror, reflecting an amount R back through the upper channel and an output amount $1 - R$ is present in the lower channel. Mirror physics is based on interference. [32]

Here, $z = 0.01$ is the propagation over 1cm to calculate the loss in dB/cm. Once the complex refractive index N_{eff} is known, it is possible to calculate the loss by using the imaginary part of the this effective refractive index.

Having now found an expression for the losses through knowledge of the complex effective refractive index N_{eff} , we will use this to estimate losses occurring in bent waveguides. A mode profile for a bent waveguide differs from that of a straight waveguide in this way that the mode profile is shifted outward, away from the direction of the bend. It can be thought of as the mode profile preferring to move in a straight line while the outer waveguide edge is pushing it inward. Consequently, the mode profile is not centered in the waveguide anymore, causing a larger part of the mode profile to travel outside the core which will cause power leakage. For such a bent mode, one will find a higher complex value for the effective refractive index N_{eff} representing the higher absorption.

5.2.2 Passive mirrors

A passive mirror can easily be constructed by taking a symmetric y-junction that acts as a 3 dB power splitter. Both output branches are connected through a loop waveguide. Any power incident on the input port of the y-junction is evenly split between the two arms and guided through the loop, maintaining coherence as their path lengths and any impurities they may encounter are equal. Once the modes enter the y-junction again they are recombined. The losses in such a passive mirror constitute the losses of the y-junction and the bend losses of the loop. It is important to keep the radius large enough so that bend losses are kept to a minimum.

5.2.3 The Sagnac mirror

A Sagnac mirror is a mirror device which is based on interference. It is built by connecting the output ports of a directional coupler by a loop, thus directing any power coming from either branch of the coupler back into the coupler's opposite branch.

Let us consider a directional coupler with a coupling coefficient $\kappa = 0.5$, as discussed in the previous chapter. Figure 5.1 shows such a directional coupler with the output arms connected through a loop. Now consider an initial field with intensity I_0 inserted into the upper waveguide of the Sagnac mirror. An amount $(1 - \kappa)I_0 = \frac{1}{2}I_0$ is left in the upper output arm after traversing the directional coupler, and will move clockwise through the

loop. At the same time, an amount $\kappa I_0 = \frac{1}{2}I_0$ leaves the lower coupler branch and traverses the loop counterclockwise. Also remember from the previous chapter that this latter field has had a phase-lag of $-\frac{\pi}{2}$ with respect to the phase of the field in the opposite branch due to the coupling process. Forced by the loop, the fields now have to traverse the coupler once more. Now consider the total intensity of the fields in the upper channel again: of the clockwise traveling field with intensity $\frac{1}{2}I_0$, another 50% has coupled back into the upper branch, resulting in a field of $\frac{1}{4}I_0$ and a phase-lag of $-\frac{\pi}{2}$ due to coupling back into the upper branch. This field in the upper branch is joined by the remainder of the counterclockwise traveling field with intensity $\frac{1}{4}I_0$ and phase-lag $-\frac{\pi}{2}$, adding up positively to $\frac{1}{2}I_0$. Now consider the lower branch again. A field of intensity $\frac{1}{4}I_0$ is joined by a field of the same intensity and a phase-lag of $-\frac{\pi}{2} - \frac{\pi}{2} = -\pi$ which destructively interferes and no light is transmitted. By conservation of energy, all of this power must be in the upper branch, meaning that this Sagnac mirror with $\kappa = 0.5$ acts as a perfect mirror.

The transmission and reflection coefficients of a Sagnac mirror are given by: [32, 33]

$$\begin{aligned} T &= (1 - 2\kappa)^2(1 - \gamma)^2 e^{-\alpha L} \\ R &= 4\kappa(1 - \kappa)(1 - \gamma)^2 e^{-\alpha L} \end{aligned} \quad (5.2)$$

Here, κ is the coupling coefficient as discussed in Chapter 4. Two loss factors attenuate the transmission T and reflection R : γ for the losses in the directional coupler, and α for the losses in the loop, where L is the length of the loop.

By tuning the coupling coefficient κ of the directional coupler, it is possible to tune the reflectivity of the Sagnac mirror. Since a $R = 1$ reflecting mirror is obtained for a coupling coefficient $\kappa = 0.5$, the coupling coefficient is $0 \leq \kappa \leq 0.5$ for $0 \leq R \leq 1$.

5.3 Simulations

5.3.1 Bend losses

Bend loss calculations were performed for a waveguide geometry as in Chapter 4, both for designed geometry and geometry found in SEM results. Figure 5.2 shows the results. As the bend radius decreases, the losses increase exponentially. It is therefore beneficial to keep the bend radius as large as possible, if space on a chip permits a large bend radius. The overall trend in Figure 5.2 is that TE bend losses are lower than TM bend losses for the geometry considered. This is due to the fact that TE has a better mode confinement. From bend loss considerations alone it is therefore advantageous to use TE polarization rather than TM polarization. To achieve the same low bend loss values for TM as for TE, the bend radius has to be increased. For bend radii beyond $350\mu m$, bend losses are found to be lower than 0.1dB/cm for all simulated geometries, and polarizations TE and TM.

5.3.2 Sagnac mirror

The behavior of a Sagnac mirror mainly depends on its directional coupler properties. The ratio of transmittance versus reflectance is entirely dependent on the coupling coefficient κ , whereas the magnitude of the reflected and transmitted light is influenced by losses in the mirror. Figure 5.3 shows the transmission and reflection of a Sagnac mirror for different loss values. The total losses consist of coupler losses and propagation losses in the loop, given by

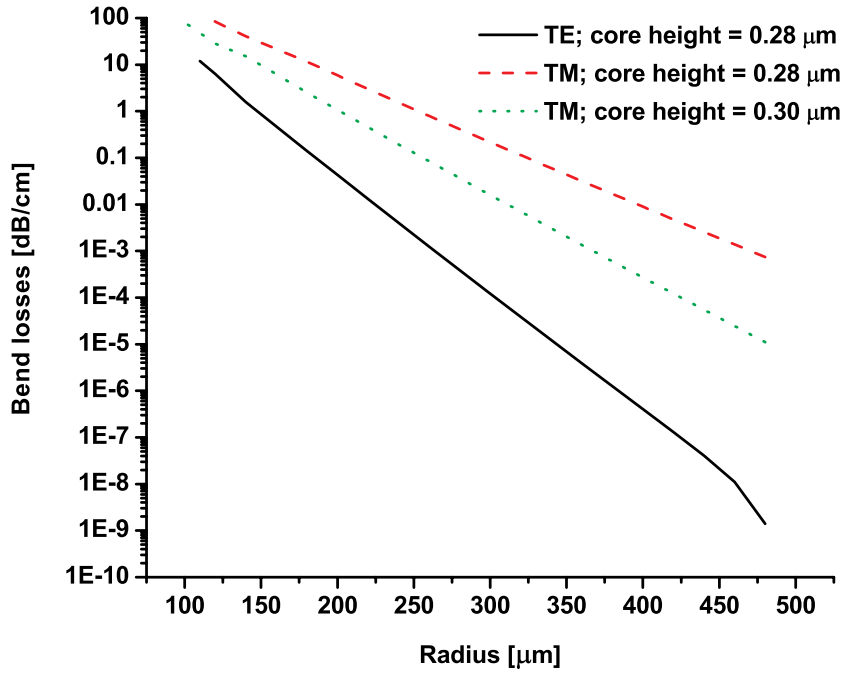


Figure 5.2: Bend losses in dB/cm as a function of waveguide bend radius. Bend losses increase exponentially as the radius is decreased. Bend losses at TM polarization exceed those for TE polarization, due to weaker confinement and stronger corresponding power leakage. Simulations at TM polarization was performed for a core height of $0.30\mu m$, as is the core height aimed for, and for a core height of $0.28\mu m$, as is the core height that was measured from SEM images. Bend losses lower than 0.01dB/cm can be expected for radii beyond $325\mu m$, for a core height of $0.30\mu m$. Simulations were carried out using the default geometry and the one measured by SEM.

$(1 - \gamma)^2 e^{-\alpha L}$ in Equation 5.2. For a Sagnac mirror without any losses, the reflectance is 100% for a coupling coefficient $\kappa = 0.5$, or 3 dB. The transmittance equals 0% for a 3 dB coupler, regardless of the loss value. A loss value of 50% reduces the reflectance by that same amount. The reflectance reduces linearly with increasing total loss value.

In chapter 4, two types of couplers were discussed. We will now employ these two couplers in a Sagnac mirror and study its behavior. Figure 5.4 shows the reflectance of two Sagnac mirrors, one that is parametrized to behave as a 100% mirror (a) and the other (b) as an 88% mirror for $L_c = L_{c0}$. The reflectance is plotted as a function of the deviation in coupling length L_c , which depends on the waveguide geometry and mode confinement, as discussed in chapter 4. The 100% mirror in Figure 5.4a shows a stunningly flat response to variations in coupling length. The reason is that for a 3 dB coupler, the Sagnac reflectance is most insensitive to variations in coupling coefficient κ , as the reflectance is at its peak value, see Figure 5.3. Here, even the Sagnac mirror with a single directional coupler structure is insensitive to $\pm 5\%$ variations in coupling length L_c . The reflectance of the Sagnac mirror with the Mach-Zehnder coupler is insensitive to $\pm 10 - 30\%$ variations in L_c , depending on the phase-shift θ .

For the mirrors designed to reflect 88%, the Sagnac mirror with the single coupler is now

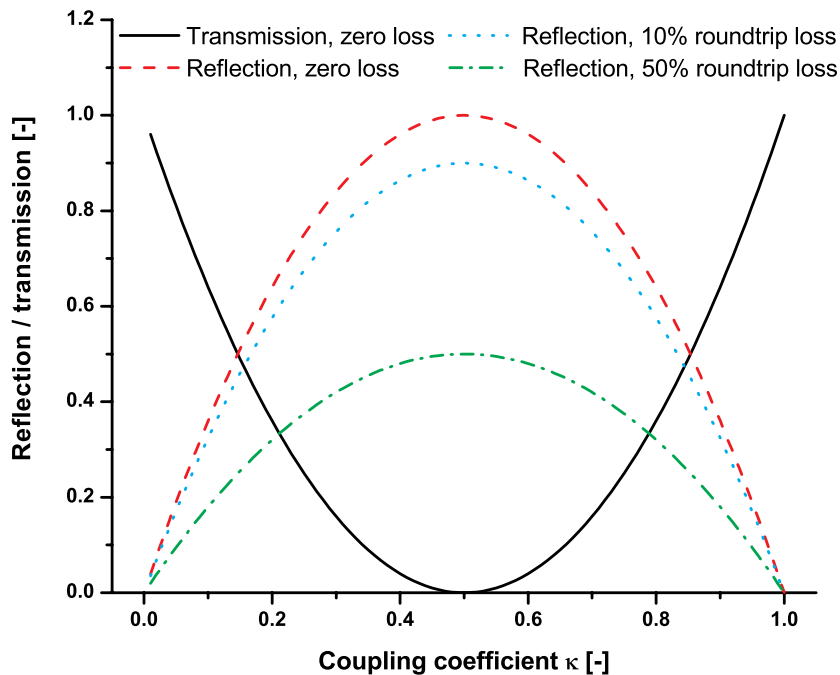


Figure 5.3: Transmission and reflection curves for a Sagnac mirror, as a function of the coupling coefficient κ of the directional coupler. Given zero loss, the reflection equals 100% for a 3 dB directional coupler. The transmission equals 0% for a 3 dB coupler. When losses, coupler losses and propagation losses are present in the Sagnac mirror, the reflection reduces linearly with the total loss value.

more sensitive to variations in L_c due to the Sagnac reflectance being more sensitive to κ . The Sagnac mirror employing a Mach-Zehnder coupler again exhibits insensitivity to variations in L_c around L_{c0} , but this depends on the phase-shift θ . Figure 5.4b bears close resemblance to Figure 4.7 in chapter 4. The difference however is that the reflectance of the Sagnac mirrors with a phase-shift θ that is different from the phase-shift θ_0 following from Mach-Zehnder design rules does not intersect at $L_c = L_{c0}$. The reason is that the Mach-Zehnder coupler used is not a 3 dB coupler. The phase-shift of a Mach-Zehnder coupler that is not a 3 dB coupler influences the coupling behavior at $L_c = L_{c0}$ while for a 3 dB coupler the phase-shift does not influence coupling at $L_c = L_{c0}$.

5.4 Conclusions

The effective refractive index of a material consists of both a real and imaginary part. The imaginary part represents losses due to absorption. The refractive indices for bent waveguides were obtained from simulations and the losses were calculated. Bend losses lower than 0.1 dB/cm were found for bend radii beyond 350 μm for TE and TM polarization.

Passive mirrors can easily be constructed using a symmetric y-junction in combination with a loop. The loop radius must be large enough in order not to end up with high losses.

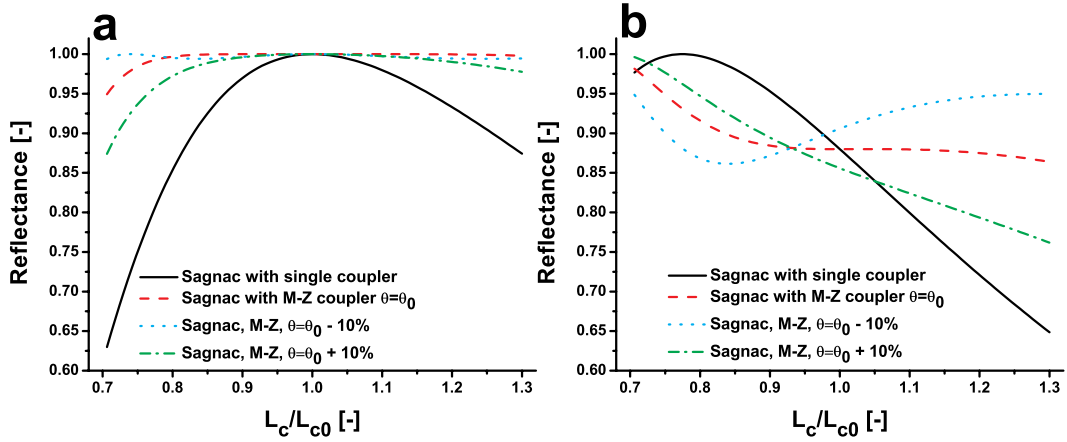


Figure 5.4: Sagnac mirror reflectance as a function of variations in coupling length L_c/L_{c0} . Figure (a) plots the behavior of Sagnac mirrors that are designed to reflect 100% of the input intensity, while (b) plots the reflectance for Sagnac mirrors designed to reflect 88% of the input intensity.

A Sagnac mirror is based on interference. The reflectance is determined by the coupling coefficient of the directional coupler. A 3 dB directional coupler yields a mirror with a reflectance of 100%.

Two types of Sagnac mirrors have been investigated. One is a Sagnac mirror that employs a standard, single directional coupler. Such a Sagnac mirror is very sensitive to variations in coupling length introduced during fabrication. Another Sagnac mirror contains a Mach-Zehnder coupler. This Sagnac mirror exhibits a reflectance that is insensitive to variations in coupling length, depending on the phase-shift.

Chapter 6

Design of on-chip laser devices

6.1 Introduction

In previous chapters, gain in Nd-doped Al_2O_3 channels has been investigated and a net gain at signal wavelength has been demonstrated. In addition, a channel waveguide laser was investigated by simulations and the results show that these channels have aptitude to support waveguide lasing. To integrate a laser on a chip, passive and active waveguide mirrors have been discussed. An integrated waveguide laser employing a Sagnac interferometer has previously been demonstrated in Erbium-doped alumino-silicate waveguides [34]. In this chapter, we will use experimental results from coupler measurements to parametrize Sagnac mirrors in order to design an integrated on-chip Nd-doped waveguide laser in Al_2O_3 . The designs have been placed on a new mask to realize the lasers on a wafer.

6.2 Exploring different laser designs

6.2.1 Sagnac-pumped integrated waveguide laser

Figure 6.1 depicts an integrated Nd-doped waveguide laser that consists of a passive mirror and a Sagnac mirror. Pump light is coupled into the upper channel. It will traverse two directional coupler devices (a) and (b), where coupler (a) is designed to couple 100% at signal wavelength. Coupler (a) will not couple any pump light, which is confirmed by experimental results in Chapter 4. Coupler (b) is part of the Sagnac mirror. Pump light will not be coupled by coupler (b) and will therefore traverse the loop in a clockwise direction, after which it will pass coupler (b) again into the straight section and passive mirror. In this way, the entire upper channel, the Sagnac loop and the passive mirror will be pumped as long as not all pump light is absorbed.

The cavity is colored black in Figure 6.1. Any signal light that is generated in the cavity will be reflected between the Sagnac mirror and the passive mirror. Only a small fraction of this signal light will escape through the Sagnac mirror, into coupler (a) where 100% is coupled into the lower signal-out waveguide channel. The Sagnac reflection is determined by coupler (b).

The cavity consists of the Sagnac mirror, the passive mirror and the straight section connecting these two. Technically, the loops are part of the mirror, but since the signal light has to traverse the loops during every roundtrip the length of the loops contributes to the

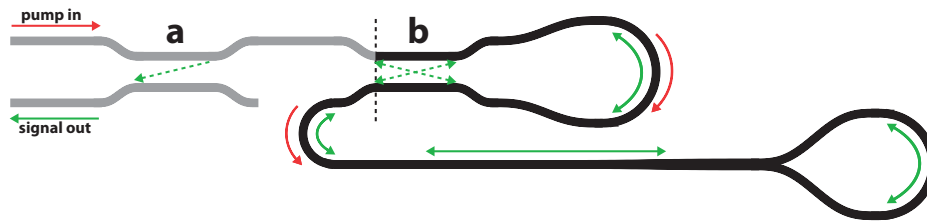


Figure 6.1: Diagram of an integrated Nd-doped waveguide laser that is pumped through the Sagnac mirror. Pump power is coupled in the upper waveguide channel and will traverse coupler (a). The Sagnac mirror is pumped and any pump power remaining will pump the straight section and passive mirror. Signal power transmitted by the Sagnac mirror will be coupled out by coupler (a). The reflectance of the Sagnac is determined by the coupling coefficient of coupler (b). The cavity is colored black.

cavity length. The roundtrip cavity length is therefore the sum of the circumference of the two loops plus twice the length of the section connecting the loops.

6.2.2 Cavity-pumped integrated waveguide laser

Figure 6.2 shows a diagram of an integrated Nd-doped waveguide laser that consists of a passive mirror and a Sagnac mirror. The difference between this design and the design in Figure 6.1 is that the light at pump wavelength only has to traverse one coupler (a). Depending on the length of the straight section and the passive mirror, most of the pump light will be absorbed in this upper channel. If any pump light is reflected back by the passive mirror through coupler (a) it will be lost since it is not coupled. Coupler (a) is designed to couple 100% at signal wavelength. All signal light that is generated in the upper, pumped, channel waveguide is therefore coupled into the Sagnac mirror. This Sagnac is not pumped, contrary to the one used in the design of Figure 6.1. Any light not reflected by the Sagnac mirror leaves the cavity through the lower waveguide channel where it can be coupled out.

The cavity is colored black in Figure 6.2. The roundtrip cavity length equals the sum of the loop circumference of the two mirrors, plus twice the length of the connecting straight and bent sections. Whereas the cavity in Figure 6.1 can potentially be pumped entirely, the

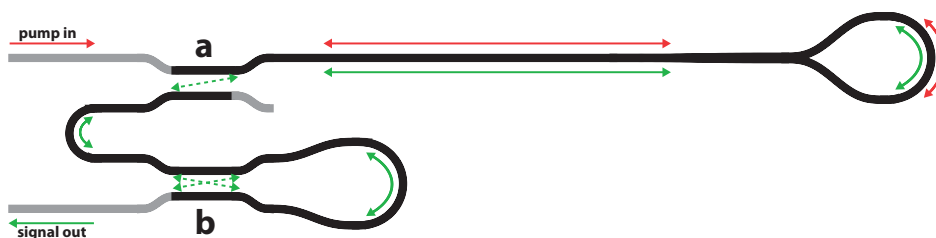


Figure 6.2: Diagram of an integrated Nd-doped waveguide laser that is pumped directly into the straight cavity section. Pump power is coupled into the upper waveguide channel and will traverse coupler (a) without coupling. All generated signal light will be coupled by coupler (a), into the Sagnac outcoupling mirror. The reflectance of the Sagnac mirror is determined by the coupling coefficient of coupler (b). Any transmitted signal light will exit the cavity through the lower waveguide channel. The sections that are colored black are part of the cavity.



Figure 6.3: Diagram of an integrated Nd-doped channel waveguide laser with a loop cavity. Pump power is coupled in the upper waveguide and will traverse coupler (a) without coupling. Laser light is generated in the cavity, (colored black) and is partially coupled out by coupler (b). Since laser light travels in the loop both clockwise and anti-clockwise, laser light is coupled into the upper channel on the right and the lower channel on the right.

cavity in Figure 6.2 can only be partially pumped in the upper channel waveguide.

Coupler (a), in Figure 6.2 is very critical to the behavior of the laser in terms of threshold pump power and slope efficiency. If coupler (a) does not couple $\kappa = 100\%$ but $\kappa = 98\%$, for instance, the roundtrip loss at signal wavelength due to coupler (a) will be $2 \times 2\%$.

The advantage of using the lay-out depicted in Figure 6.2 is that pump light only experiences coupler losses due to one coupler (a) in the cavity. In Figure 6.1, the pump light in the cavity experiences three times the coupler losses, and five times the coupler losses in case a Mach-Zehnder coupler is used for the Sagnac mirror.

6.2.3 Ringlaser

An alternative laser cavity design for a Nd-doped waveguide laser is displayed in Figure 6.3. This is a modified version of an Erbium-doped waveguide laser demonstrated by Bradley et al. [23], to investigate the laser light intensity of the laser channel mode traveling in a clockwise direction compared to the one traveling in an anti-clockwise direction. Pump light is coupled into the upper channel on the left and will traverse couplers (a) and (b), which are designed to couple only laser light at 1064 nm. The entire loop will be pumped as long as the length of the loop is not significantly longer than the pump absorption length.

Laser light will be generated in the loop and will traverse the loop in clockwise and anti-clockwise direction. A fraction of the laser light is coupled out by coupler (b), into the channels on the right. Coupler (a) is designed to couple 100% of the laser light to minimize cavity losses.

6.3 Laser parametrization

6.3.1 Waveguide dimensions and cavity length

The Nd-doped Al_2O_3 channel waveguide dimensions used for the designed lasers is $1.2 \mu\text{m}$ for the channel width and $0.3 \mu\text{m}$ for the channel height. These values have been chosen because those were the dimensions of the channels of the measured couplers. In Chapter 4 we have seen that these channel dimensions support only the fundamental mode at signal wavelength,

1064 nm, which is desirable for laser operation.

The cavity length for the Nd-doped Al_2O_3 waveguide lasers has been determined using the pump absorption length. Since the passive mirrors used in the designs depicted in Figures 6.1 and 6.2 also reflect pump light, the roundtrip cavity length can be chosen to match the absorption length. The absorption length for different concentrations have been determined and are given in Table 6.1, for two values of the absorption cross-section σ_a . The highest $1/e^2$ absorption length is 2.53 cm for the lowest Nd concentration and the lowest $1/e^2$ absorption length is 0.68 cm for the highest Nd concentration. Based on this, a roundtrip cavity length of 1.5 cm was selected for the laser with the shortest cavity and a roundtrip cavity length of 2.5 cm was selected for the laser with the longest cavity. Selecting a much longer cavity length will only add additional background loss as no signal light at 1064 nm is reabsorbed by the four-level Nd^{3+} -system.

Table 6.1: $1/e$ and $1/e^2$ absorption lengths for two values of the absorption cross-section σ_a and the concentrations for which gain was measured in Chapter 2.

Nd concentration ($\times 10^{20}$) [cm^{-3}]	absorption length for $\sigma_a = 0.7 \cdot 10^{-20} \text{cm}^2$		absorption length for $\sigma_a = 1.0 \cdot 10^{-20} \text{cm}^2$	
	[cm] ($1/e$)	[cm] ($1/e^2$)	[cm] ($1/e$)	[cm] ($1/e^2$)
1.13	1.26	2.53	0.89	1.77
1.38	1.04	2.07	0.72	1.45
1.68	0.85	1.70	0.60	1.19
2.27	0.63	1.26	0.44	0.88
2.95	0.48	0.97	0.34	0.68

6.3.2 Mirror reflectivities

A maximum internal net gain of 1.6 dB/cm has been assumed, which yields a roundtrip gain of 2.4 dB/cm for a 1.5 cm roundtrip cavity length. A value of 1 dB has been assumed for the loss of the passive mirror plus additional coupler losses of 0.2 dB. The maximum loss of the mirrors was thus estimated to be 1 dB. If one mirror is set to 100% coupling, the other mirror is allowed a loss of 1 dB, or a reflectivity of 80%.

Nd-doped Al_2O_3 waveguide lasers have been designed with mirror reflectivities of 99% down to 88%. Sagnac mirrors with these reflectivities were designed with single directional couplers and Mach-Zehnder directional couplers, as discussed in Chapter 4. The Sagnac mirrors with the Mach-Zehnder couplers were designed according to the design rules given in Chapter 4, to yield mirrors that are insensitive to a wide range of fabrication errors. The Sagnac mirrors with the single directional couplers have designed reflectivities of 99% down to 94%.

A coupling length of $L_{c0} = 253 \mu\text{m}$ has been assumed for the couplers, based on measured results in Chapter 4. For the Sagnac mirrors with the single directional coupler, the physical length of the couplers was chosen to obtain mirror reflectivities of 99, 98 and 94%, shown in Figure 6.4a. If, due to fabrication errors, the coupling length L_c changes, the resulting mirror

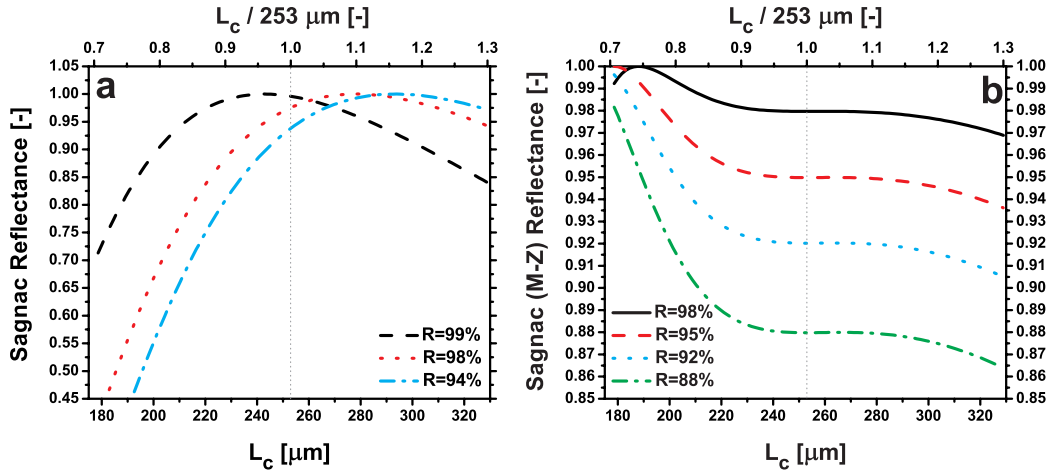


Figure 6.4: Plots of the designed mirror reflectivities for a Sagnac mirror with a single directional coupler (a), and a Sagnac mirror with a Mach-Zehnder, balanced coupler, (b).

reflectivities change according to the curves in Figure 6.4a.

The reflectivities of the Sagnac mirrors with the balanced couplers have been set at 98, 95, 92 and 88%. Their response to deviations from the measured L_{c0} has been shown in Figure 6.4b. Since the performance of a balanced Sagnac mirror also depends on the phase-shift, variations of $\pm 5\%$ in the phase-shift have been included in the mask design.

6.3.3 Signal-out couplers

In Figure 6.1, coupler (a) is designed to couple out all signal light from the upper waveguide channel into the lower channel. This coupler is not critical to laser operation, as it is not part of the cavity. However, it is desirable for this coupler to have a coupling coefficient $\kappa = 1$, or 100% coupling, since any laser light that is not extracted from the upper channel is lost. The coupler indicated by (a) in Figure 6.1 was hence set to 100%, but no variations for this coupler have been included on the mask.

Coupler (a) in Figure 6.2, however, is critical to laser operation. Therefore, variations in the physical coupler length for coupler (a) have been included on the mask. In Figure 6.5, the coupling coefficients of three couplers are plotted. These couplers have been designed in such a way that their coupling coefficients overlap at 96%, to obtain a coupling coefficient $\geq 96\%$ across a $\pm 30\%$ variation in coupling length L_c . In this way, a laser with a roundtrip loss of less than 0.35 dB due to coupler (b) in Figure 6.2 will be realized on the chip.

A similar approach has been used to parametrize coupler (a) of the loop cavity in Figure 6.3.

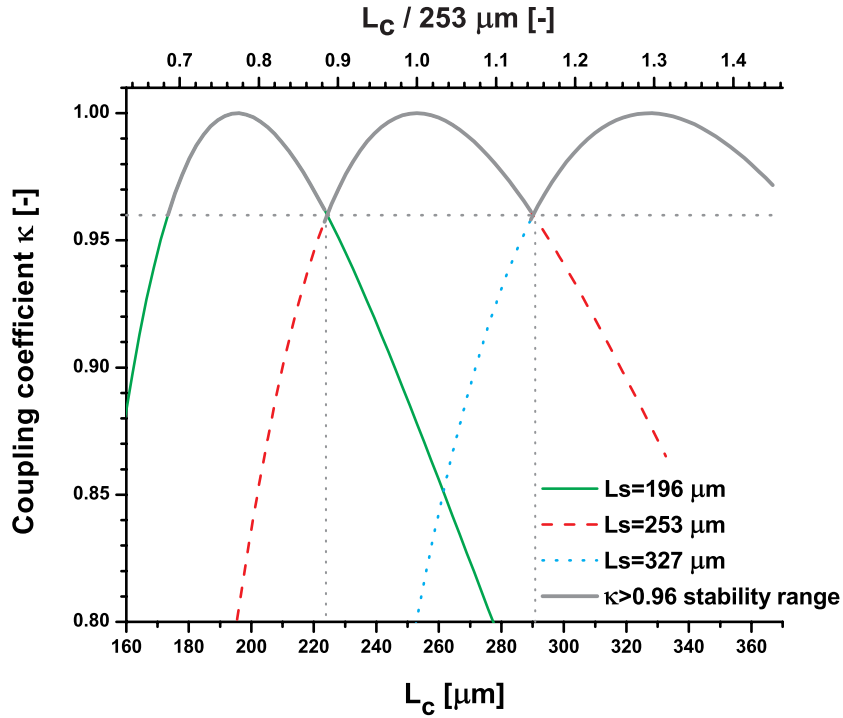


Figure 6.5: Coupling coefficients as a function of coupling length L_c . These couplers are designed to couple a maximum amount of laser light between the passive mirror and the Sagnac mirror in Figure 6.2. A set of three couplers have been designed in such a way that for a $\pm 30\%$ deviation of coupling length L_c due to fabrication errors, one of the three couplers exceeds a coupling coefficient of 96%.

6.4 Conclusions

Three integrated Nd-doped waveguide lasers have been designed. Two of these consist of a passive mirror and a Sagnac mirror, which is used to couple out laser light. One of these Sagnac-type waveguide lasers is pumped through the Sagnac mirror, whereas the other Sagnac-type waveguide laser is being pumped through the passive mirror. The latter Sagnac-type waveguide laser requires a coupler within the cavity to couple laser light between the passive and Sagnac mirror. The third integrated Nd-doped waveguide laser uses a loop cavity.

Based on a maximum internal net gain of 1.6 dB/cm, mirror reflectivities of 99% down to 88% have been used as reflectivities for the Sagnac mirrors.

Conclusions

In this thesis, gain in Nd-doped Al_2O_3 waveguide channels has been demonstrated. For a Nd concentration of $1.68 \cdot 10^{20} \text{ cm}^{-3}$, 4.0 dB of internal net gain has been measured in 1-cm-long waveguide channels, and this gain is competitive with other Nd-doped materials. The observed gain is sufficient for integrated $\text{Al}_2\text{O}_3:\text{Nd}^{3+}$ channel waveguide amplifiers and channel waveguide lasers.

An integrated channel waveguide laser was modeled by rate equations and numerically analyzed. In this simulation, different mirror reflectivities were used. A mirror reflectivity of 88% results in a threshold pump power of 1.8 mW and a slopy efficiency of 15.2%, for waveguides and Nd concentrations comparable to the ones measured in this thesis.

In order to design an on-chip channel waveguide laser, channel waveguides and couplers have been analyzed by simulations and compared to experimental results. Waveguide channels studied in this thesis only support the fundamental mode at 1064 nm, which is the laser wavelength. Coupler structures have been simulated and measured. Measured results deviate from simulated coupler behavior, due to a difference in channel geometry introduced during fabrication. This was verified by SEM imaging. In order to minimize sensitivity to fabrication errors, a cascaded directional coupler was studied by simulation and the results show a high insensitivity to fabrication errors.

In order to fabricate an on-chip integrated waveguide laser, passive and active mirrors have been discussed. The active mirror is a Sagnac mirror, which is based on interference. Sagnac mirrors based on single directional couplers and Mach-Zehnder couplers have been discussed. The results from simulations show that the Sagnac mirror based on a Mach-Zehnder coupler structure is most insensitive to fabrication errors.

Different integrated Nd-doped Al_2O_3 channel waveguide lasers have been discussed and have been realized on a mask design. Two of these integrated waveguide lasers employ Sagnac mirrors, while another type consists of a loop cavity.

Bibliography

- [1] S.E. Miller. Integrated optics - an introduction. *Bell System Techn. J.*, 48:2059–2069, 1969.
- [2] R.V. Pole, S.E. Miller, J.H. Harris, and P.K. Tien. Integrated optics and guided waves - a report of the topical meeting. *Applied Optics*, 11(8), 1972.
- [3] E. Krioukov, D.J. W. Klunder, A. Driessen, J. Greve, and C. Otto. Sensor based on an integrated optical microcavity. *Opt. Lett.*, 27(7):512–514, 2002. URL <http://ol.osa.org/abstract.cfm?URI=ol-27-7-512>.
- [4] Katrien De Vos, Peter Debackere, Tom Claes, Jordi Girones, Wout De Cort, Etienne Schacht, Roel G. Baets, and Peter Bienstman. Label-free biosensors on silicon-on-insulator optical chips. volume 7397, page 739710. SPIE, 2009. doi: 10.1117/12.825648. URL <http://link.aip.org/link/?PSI/7397/739710/1>.
- [5] J. Hübner, K.B. Mogensen, A.M. Jorgensen, P. Friis, P. Telleman, and J.P. Kutter. Integrated optical measurement system for fluorescence spectroscopy in microfluidic channels. *Review of scientific instruments*, 72(1), 2001.
- [6] Chaitanya Dongre, Ronald Dekker, Hugo J. W. M. Hoekstra, Markus Pollnau, Rebeca Martinez-Vazquez, Roberto Osellame, Giulio Cerullo, Roberta Ramponi, Rob van Weeghel, Geert A. J. Besselink, and Hans H. van den Vlekert. Fluorescence monitoring of microchip capillary electrophoresis separation with monolithically integrated waveguides. *Opt. Lett.*, 33(21):2503–2505, 2008. URL <http://ol.osa.org/abstract.cfm?URI=ol-33-21-2503>.
- [7] E.A.J. Marcatili. Dielectric rectangular waveguide and directional coupler for integrated optics. *Bell System Techn. J.*, 48(2071), 1969.
- [8] B. S. Kawasaki, K. O. Hill, D. C. Johnson, and Y. Fujii. Narrow-band bragg reflectors in optical fibers. *Opt. Lett.*, 3(2):66–68, 1978. URL <http://ol.osa.org/abstract.cfm?URI=ol-3-2-66>.
- [9] F. Ay, J.D.B. Bradley, R.M. de Ridder, K. Wörhoff, and M. Pollnau. Bragg gratings in Al₂O₃ channel waveguides by focused ion beam milling. In *Proceedings Symposium IEEE/LEOS Benelux Chapter*. University of Twente, 2008.
- [10] E.J Post. Sagnac effect. *Rev. Mod. Phys.*, 39(2):475–493, Apr 1967. doi: 10.1103/RevModPhys.39.475.

- [11] M.K. Smit, G.A. Acket, and C.J. van der Laan. Al_2O_3 films for integrated optics. *Thin Solid Films*, 138(2):171 – 181, 1986. ISSN 0040-6090. doi: DOI:10.1016/0040-6090(86)90391-3. URL <http://www.sciencedirect.com/science/article/B6TW0-46TY9VR-64/2/955ab89306a5bfaf5cda4a988800e650>.
- [12] J.D.B. Bradley, F. Ay, K. Wörhoff, and M. Pollnau. Fabrication of low-loss channel waveguides in Al_2O_3 and Y_2O_3 layers by inductively coupled plasma reactive ion etching. *Applied Physics B*, 89(2-3):311–318, 2007.
- [13] E. Lallier, J.P. Pocholle, M. Papuchon, M.P. DeMicheli, M.J. Li, Q. He, D.B. Ostrowsky, C. Grezes-Besset, and E. Pelletier. Nd:MgO:LiNbO₃ channel waveguide laser devices. *Quantum Electronics, IEEE Journal of*, 27(3):618–625, Mar 1991. ISSN 0018-9197. doi: 10.1109/3.81371.
- [14] Y. Sikorski, A.A. Said, P. Bado, R. Maynard, C. Florea, and K.A. Winick. Optical waveguide amplifier in nd-doped glass written with near-IR femtosecond laser pulses. *Electronics Letters*, 36(3), 2000.
- [15] Asher Peled, Menachem Nathan, Alexander Tsukernik, and Shlomo Ruschin. Neodymium doped sol-gel tapered waveguide amplifier. *Applied Physics Letters*, 90(16):161125, 2007. doi: 10.1063/1.2730577. URL <http://link.aip.org/link/?APL/90/161125/1>.
- [16] Jing Yang, Mart B. J. Diemeer, Dimitri Geskus, Gabriël Sengo, Markus Pollnau, and Alfred Driessen. Neodymium-complex-doped photodefined polymer channel waveguide amplifiers. *Opt. Lett.*, 34(4):473–475, 2009. URL <http://ol.osa.org/abstract.cfm?URI=ol-34-4-473>.
- [17] M. Pollnau, P.J. Hardman, M.A. Kern, W.A. Clarkson, and D.C. Hanna. Upconversion-induced heat generation and thermal lensing in Nd:YLF and Nd:YAG. *Physical Review B*, 58(24):16076–16092, 1998.
- [18] K. Wörhoff, J.D.B. Bradley, F. Ay, D. Geskus, T.P. Blauwendraat, and M. Pollnau. Reliable low-cost fabrication of low-loss $\text{Al}_2\text{O}_3:\text{Er}^{3+}$ waveguides with 5.4-dB optical gain. *IEEE Journal of Quantum Electronics*, 45(5), May 2009.
- [19] Jing Yang. Absorption and emission cross-sections for Nd. .
- [20] O. Svelto. *Principles of Lasers*. Plenum Press, New York, 4th edition, 1976.
- [21] Bahaa E.A. Saleh and Malvin Carl Teich. *Fundamentals of Photonics*. Wiley-Interscience, 1991.
- [22] Jing Yang. Slab waveguide losses at 1064 nm. .
- [23] J.D.B. Bradley, R. Stoffer, L. Agazzi, F. Ay, K. Wörhoff, and M. Pollnau. Integrated $\text{Al}_2\text{O}_3:\text{Er}^{3+}$ ring lasers on silicon with wide wavelength selectivity. Submitted to *Optics Express* (2009).
- [24] M. Pollnau, P.J. Hardman, W.A. Clarkson, and D.C. Hanna. Upconversion, lifetime quenching, and ground-state bleaching in $\text{Nd}^{3+}:\text{LiYF}_4$. *Optics Communications*, 147: 203–211, 1998.

-
- [25] Markus Pollnau. Numerical analyzation software, version 62.
- [26] Laura Agazzi. Lifetime measurements of the $^4F_{3/2}$ level of the Nd^{3+} ion.
- [27] Y. Guyot, H. Manaa, J. Y. Rivoire, R. Moncorgé, N. Garnier, E. Descroix, M. Bon, and P. Laporte. Excited-state-absorption and upconversion studies of Nd^{3+} -doped single crystals $Y_3Al_5O_{12}$, $YLiF_4$, and $LaMgAl_{11}O_{19}$. *Phys. Rev. B*, 51(2):784–799, Jan 1995. doi: 10.1103/PhysRevB.51.784.
- [28] Katsunari Okamoto. *Fundamentals of Optical Waveguides*. Academic press, 2 edition, 2005.
- [29] Theodor Tamir, Giora Griffel, and Henry L. Bertoni, editors. *Guided-Wave Optoelectronics: Device Characterization, Analysis and Design*. Springer, 1995.
- [30] Thomas E. Murphy, Brent E. Little, and Henry I. Smith. Wavelength- and polarization-insensitive integrated directional couplers using mach-zehnder structures. In *Integrated Photonics Research*, page RTuA5. Optical Society of America, 1999. URL <http://www.opticsinfobase.org/abstract.cfm?URI=IPR-1999-RTuA5>.
- [31] Brent E. Little and Tom Murphy. Design rules for maximally flat wavelength-insensitive optical power dividers using mach-zehnder structures. *IEEE Photonics Technology Letters*, 9(12):1607–1609, 1997.
- [32] David B. Mortimore. Fiber loop reflectors. *Journal of Lightwave Technology*, 6(7):1217–1224, 1988.
- [33] Paul Urquhart. Fiber lasers with loop reflectors. *Applied Optics*, 28(17):3759–3770, 1989.
- [34] Hyunil Byun, Dominik Pudo, Sergey Frolov, Amir Hanjani, Joseph Shmulovich, Erich P. Ippen, and Franz X. Kartner. Integrated, low-jitter, 400 mhz femtosecond waveguide laser. In *LEOS Annual Meeting*. LEOS, 2008.

Appendix A

Integrated laser designs

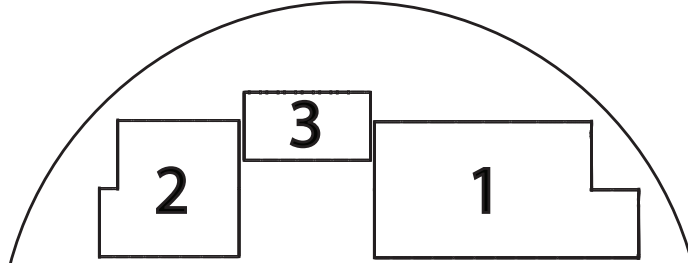


Figure A.1: Diagram of the wafer areas at which the chips are placed. The two L-shaped regions consist of two rows of chips. The arc represents the top half of a wafer.

A.1 General information

Each of the designed chips is numbered by a binary code, consisting of 7 rectangles, in which a big rectangle represents a binary '1' and a small rectangle represents a binary '0'. Whenever 'wafer area' is mentioned in the tables in this appendix, this refers to the wafer sections indicated in Figure A.1. All chips, except the chips with the test-structures for the loop-mirrors, contain two straight waveguides for reference purposes. Furthermore, directional coupler structures that have been used in laser designs have been repeated on that same chip for characterization purposes. Waveguide dimensions and minimum bend radii are presented in Table A.1, while the next sections present specific information about the various laser chip designs. Whenever a phase-shift $\Delta\theta$ is mentioned in this appendix, a phase-shift relative to the optimized phase-shift 2θ is meant, as given by Equations 4.7 and 4.8 in Chapter 4.

Table A.1: General chip properties

parameter	unit	value
desired Al_2O_3 layer thickness	$[\mu\text{m}]$	0.3
minimum channel separation	$[\mu\text{m}]$	100
minimum bend radius	$[\mu\text{m}]$	375
waveguide width	$[\mu\text{m}]$	1.2
chip length	$[\text{mm}]$	8.5
chip height	$[\text{mm}]$	1.9 - 3.4

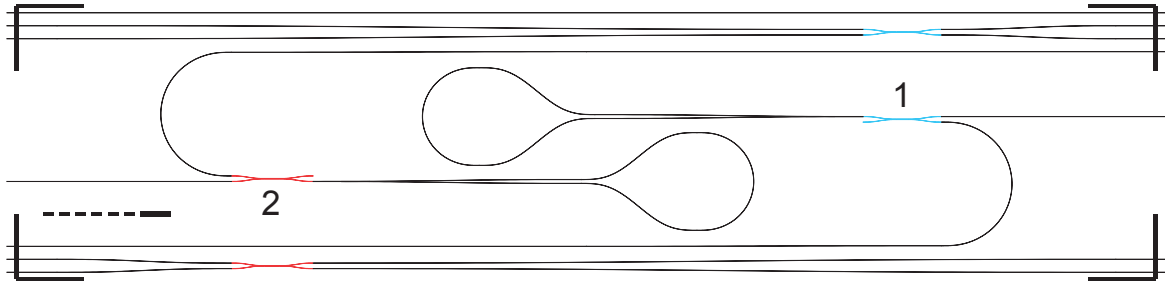


Figure A.2: Layout of a chip with loop mirrors.

A.2 Loop mirrors

Figure A.2 shows the layout of a chip containing loop mirrors. One chip contains two of these mirrors. Variation data is presented in Table A.2.

Table A.2: Variation data for chips with loop mirrors.

chip nr.	wafer area	coupler 1	coupler 2
		κ	κ
1	1	50%	65%
1	2	35%	50%

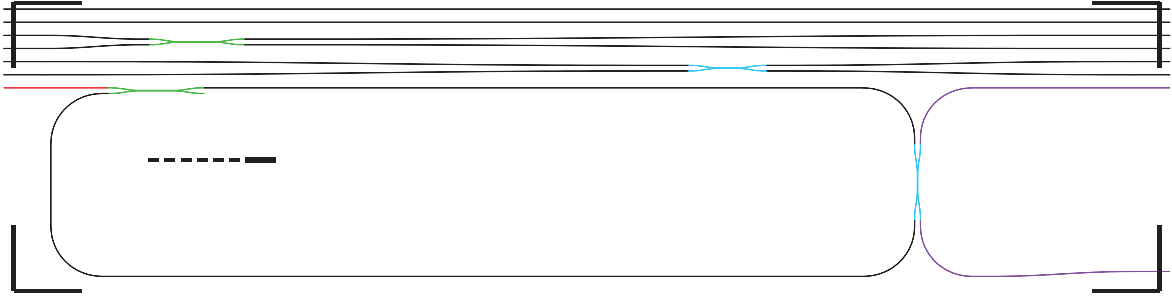


Figure A.3: Ringlasers with two signal-out waveguides (purple) to measure difference in clockwise and anti-clockwise traveling laser modes. Pump incoupling (red) on the left. Both the loop-coupler (green) and the signal-out coupler (blue) were repeated on the chip to be able to measure their coupling behavior.

A.3 Ringlaser

Figure A.3 shows the layout of a ringlaser. Each ringlaser has a *roundtrip* cavity length of 1.5 cm. Pump light is supplied through the upper left channel (red) in Figure A.3, while laser light can be outcoupled from the channels on the right (purple). Both the directional coupler in the loop (green) and the outcoupling directional coupler (blue) have been repeated on the chip to allow characterization of the couplers. Information on the variations of the designed chips has been supplied in Table A.3. This chip was designed to measure differences between clockwise and anti-clockwise traveling modes

Table A.3: Overview of ringlaser variations.

chip nr.	wafer area	loopcoupler	outcoupling mirror
		κ	R
1	3	98%	94%
2	3	96%	94%
3	3	98%	92%
4	3	96%	92%
5	3	98%	90%
6	3	96%	90%

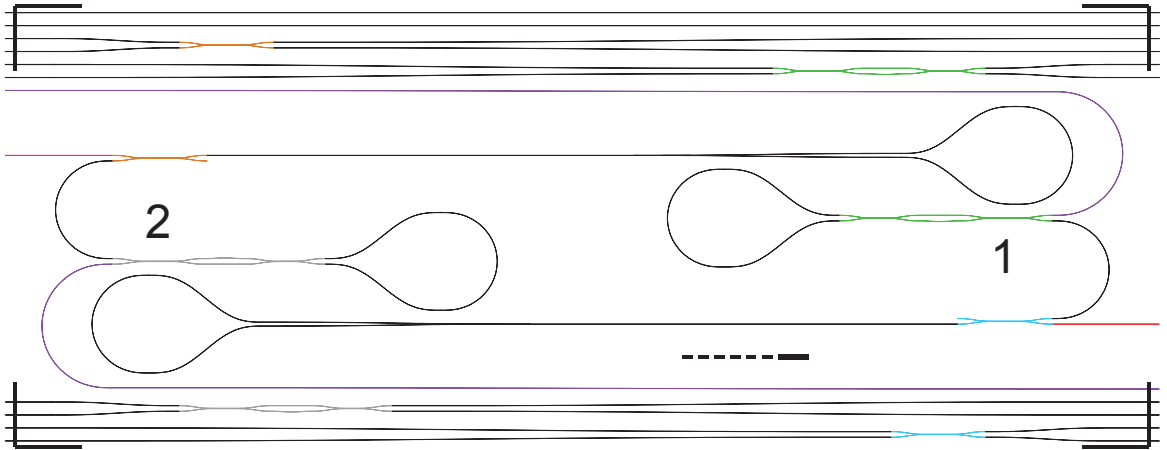


Figure A.4: Diagram of a long-cavity laser with Mach-Zehnder directional couplers in the Sagnac mirror. These lasers are pumped through the loop-mirror.

A.4 Long Sagnac laser I

Figure A.4 shows the layout of a chip which contains two laser structures with a Sagnac mirror. The Sagnac mirrors contain a Mach-Zehnder directional coupler structure. In these laser designs, only the loop mirrors are pumped and pump light is supplied in the channel indicated by the red color. The *roundtrip* cavity length is 2.4 cm, while only 1.5 cm can be pumped, since pump light will not couple into the Sagnac structure. Both laser structures on this chip are identical, except for the phase-shifts introduced in the Mach-Zehnder directional coupler for the Sagnac mirrors. $\Delta\theta_1$ and $\Delta\theta_2$ are the Mach-Zehnder phase-shifts for lasers 1 and 2, respectively. Information on the variations has been given in Table A.4.

Table A.4: Overview of variations in the long cavity Sagnac lasers with Mach-Zehnder directional couplers.

chip nr.	wafer area	cavity coupler	sagnac mirror		
		κ	R	$\Delta\theta_1$	$\Delta\theta_2$
10	1	88%	98%	-5%	+5%
11	1	100%	98%	-5%	+5%
12	1	80%	98%	-5%	+5%
13	1	88%	95%	-5%	+5%
14	1	100%	95%	-5%	+5%
15	1	80%	95%	-5%	+5%
16	1	88%	92%	-5%	+5%
17	1	100%	92%	-5%	+5%
18	1	80%	92%	-5%	+5%
19	1	88%	88%	-5%	+5%
20	1	100%	88%	-5%	+5%

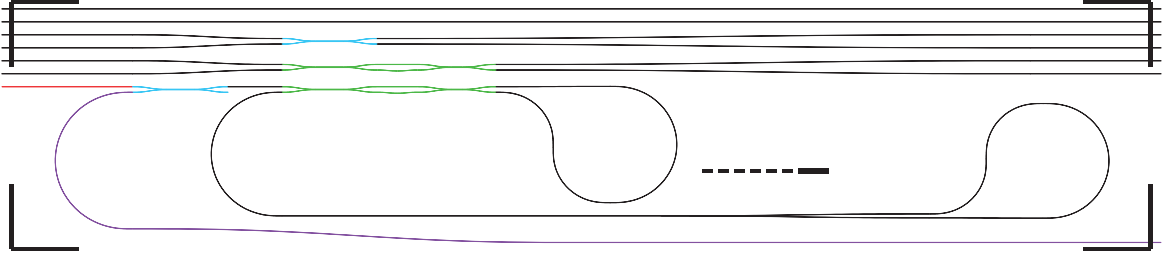


Figure A.5: Diagram of a long-cavity laser with a Mach-Zehnder directional coupler in the Sagnac mirror. These lasers are pumped through the Sagnac mirror.

A.5 Long Sagnac laser II

The layout of a long-cavity laser structure employing a Sagnac mirror with a Mach-Zehnder coupler is shown in Figure A.5. This laser structure has a *roundtrip* cavity length of 2.35 cm, which can be entirely pumped provided enough pump light is supplied. Information on the variations is given in Table A.5.

Table A.5: Overview of variations in the long cavity Sagnac lasers with a Mach-Zehnder directional coupler.

chip nr.	wafer area	signal-out coupler	sagnac mirror	
		κ	R	$\Delta\theta$
5	2	100%	98%	-5%
6	2	100%	98%	0%
7	2	100%	98%	+5%
8	2	100%	95%	-5%
9	2	100%	95%	0%
10	2	100%	95%	+5%
11	2	100%	92%	-5%
12	2	100%	92%	0%
13	2	100%	92%	+5%
14	2	100%	88%	-5%
15	2	100%	88%	0%
16	2	100%	88%	+5%

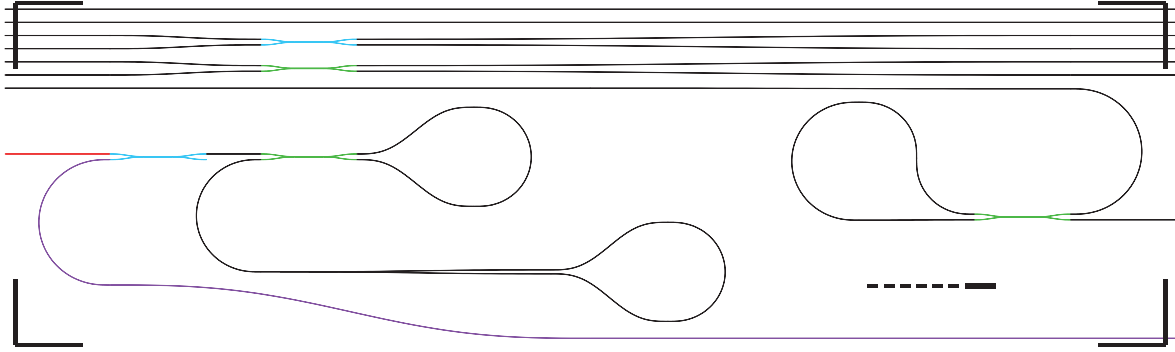


Figure A.6: Layout of the short-cavity Sagnac lasers. The Sagnac mirror contains a single directional coupler. A second Sagnac mirror with the same reflectivity is placed opposite of the laser on the chip.

A.6 Short Sagnac laser I

Figure A.6 shows the layout of a short Sagnac laser which is built with only one directional coupler. The Sagnac mirror is repeated on the same chip for characterization purposes. The *roundtrip* cavity length of the laser is 1.5 cm. The laser will need to be pumped into the upper left channel (red), directly into the Sagnac mirror. Information about the variations on the mask are given in Table A.6.

Table A.6: Overview of variations of the short-cavity lasers with a single directional coupler Sagnac mirror.

chip nr.	wafer area	signal-out coupler	sagnac mirror
		κ	R
2	2	100%	100%
7	3	100%	99%
3	2	100%	98%
4	2	100%	94%

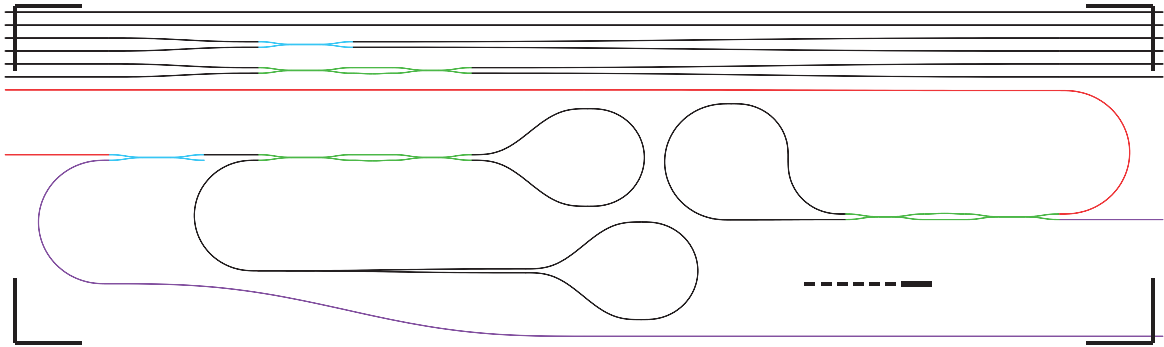


Figure A.7: Diagram of a short-cavity Sagnac laser. The Sagnac mirror consists of a Mach-Zehnder directional coupler. A second Sagnac mirror with the same properties as the one used in the laser has been placed on the right of the chip.

A.7 Short Sagnac laser II

Figure A.7 shows the layout of a short Sagnac laser with a Sagnac mirror that is made with a Mach-Zehnder directional coupler. The Sagnac mirror is repeated on the same chip for characterization purposes. The *roundtrip* cavity length of the laser is 1.65 cm. The laser will need to be pumped into the upper left channel (red), directly into the Sagnac mirror. Information about the variations on the mask are given in Table A.7.

Table A.7: Overview of variations of the short-cavity lasers with a Mach-Zehnder directional coupler Sagnac mirror.

chip nr.	wafer area	signal-out coupler	sagnac mirror		
			κ	R	$\Delta\theta$
2	1	100%	98%	-5%	
3	1	100%	98%	+5%	
4	1	100%	95%	-5%	
5	1	100%	95%	+5%	
6	1	100%	92%	-5%	
7	1	100%	92%	+5%	
8	1	100%	88%	-5%	
9	1	100%	88%	+5%	

Appendix B

Laser simulation parameters

Table B.1 below shows the parameters that were used to simulate a Nd-doped Al₂O₃ channel waveguide laser in Chapter 3.

Table B.1: The set of parameters that were used to simulate a Nd-doped channel waveguide laser in Chapter 3.

parameter	unit	value
pump beam radius	μm	0.5
laser beam radius	μm	0.5
l	mm	12.5
l_{cav}	mm	12.5
τ_1	ns	20
$\tau_{2,3,5,6,7,8}$	ns	50
T	K	288
β_{43}	-	0.378
β_{42}	-	0.075
β_{41}	-	0.339
β_{40}	-	0.209
W_c	$\text{cm}^3 \text{s}^{-1}$	1.7×10^{-16}
α (1064 nm)	dB cm^{-1}	0.9
α (800 nm)	dB cm^{-1}	0.9
σ_a	cm^2	1.0×10^{-20}
σ_e	cm^2	1.9×10^{-20}